ABSTRACT

XU, SIQI. A Novel Ultra-light Structure for Radiation Shielding. (Under the direction of Mohamed A. Bourham and Afsaneh Rabiei.)

The purpose of this research has been to design and investigate the applicability of a novel ultra-light structure to meet today's need for efficient, lightweight and multifunctional radiation shielding materials. A unique class of material, metal foams, has been studied in this work, the first time for which to be considered in the radiation shielding applications. A structure which consists of a plastic container and open-cell aluminum foams has been designed and investigated for its nuclear radiation shielding properties.

The research involves investigation of this structure for its attenuation ability of gamma-ray and thermal neutron based on measurements and analyses. The experimental work includes gamma-ray attenuation measurements and thermal neutron measurements, both of which were carried out in transmission geometries. The gamma-ray attenuation measurements were performed with a 2 mCi Cesium-137 source and a 1.2 mCi Cobalt-60 source. The thermal neutron attenuation measurements were conducted at the NCSU PULSTAR Reactor Beam port #5. By filling water and boric acid solution with different concentrations into the open-cell foams, the attenuated intensities were measured. The attenuations of the beams were calculated and compared among different types of samples with different thicknesses.

Results of the tests have revealed the improved attenuation ability of metal foams filled with fluids compared to bulk materials, as well as weight-saving advantages. Potential applications in radiation shielding have been implied.

A Novel Ultra-light Structure for Radiation Shielding

by
Siqi Xu

A thesis submitted to the Graduate Faculty of
North Carolina State University
in partial fulfillment of the
requirements for the Degree of
Master of Science

Nuclear Engineering

Raleigh, North Carolina

2008

APPROVED BY:

_____
Man-Sung Yim

_____ _____
Mohamed A. Bourham (Chair of Advisory Committee)
Afsaneh Rabiei (Co-chair of Advisory Committee)

BIOGRAPHY

Siqi Xu was born on the 11th of November 1984. She was raised in Huai'an, Jiangsu Province, China.

In June of 2002, the author graduated from Huaiyin High School and that following fall she began attending the Xi'an Jiaotong University located in Xi'an. In June of 2006 the author received her Bachelor's degree in Nuclear Engineering.

The author began graduate studies in nuclear engineering at North Carolina State University in August of 2006.

ACKNOWLEDGEMENTS

The author would like to thank Dr. Mohamed A. Bourham for his continuous guidance and support throughout the course of this work, without which, none of this would have been possible.

The author would also like to thank Dr. Afsaneh Rabiei for her guidance, support and advice throughout the work. She appreciates the opportunity granted to her with this project.

The author would like to express her gratitude to Dr. Man-Sung Yim who agreed to spend his time becoming her committee member and guided her in this work.

Thanks should also be given to Douglas David Di Julio II for both his patience and for providing continuous assistance and advice throughout different stages of the work. The thanks should also be extended to Kaushal Kishor Mishra and Mr. Mark Barefoot.

The author would also like to thank Mr. Gerald Wicks, Mr. Andrew Cook, Mr. Larry Broussard, Mr. Kerry Kincaid, and the rest of the staff at the NCSU PULSTAR reactor for their assistance during the experimental work.

Last but not the least, the author would like to thank the faculty of the Department of Nuclear Engineering and fellow colleagues for providing her the opportunity and assistance during her stay at NCSU.

Finally, the author would like to thank her family for their continuous support throughout all stages of her education.

Support for this work was provided by Department of Nuclear Engineering and North Carolina Space Grant Consortium.

TABLE OF CONTENTS

LIST OF TABLES

LIST OF FIGURES

Chapter 1 Introduction to Radiation Shielding Materials

1.1 Introduction to Radiation Shielding

The word *radiation* was used until about 1900 to describe electromagnetic waves. Today, radiation refers to the whole electromagnetic spectrum as well as to the atomic and subatomic particles that have been discovered [1]. One of the many ways in which different types of radiation are grouped is in terms of ionizing and nonionizing radiation. The word ionizing refers to the ability to ionize an atom or a molecule of the medium it traverse [1].

Nonionizing radiation is electromagnetic radiation with wavelength λ of about 10 nm or longer. This part of the electromagnetic spectrum includes radiowaves, microwaves, visible light (λ = 770-390 nm), and ultraviolet light (λ = 390-10nm).

Ionizing radiation includes the rest of the electromagnetic spectrum (X-rays, $\lambda \approx$ 0.01-10 nm) and γ-rays with wavelength shorter than that of X-rays. It also includes all the atomic and subatomic particles, such as electrons, positrons, protons, alphas, neutrons, heavy ions, and mesons.

The ionizing radiations are commonly classified into two principal types. Directly ionizing radiations include radiations of energetic particles carrying an electric charge, such as beta particles, alpha particles, protons, and other recoil nuclei. They cause ionization by direct action on electrons in atoms of the media through which they pass. Another type of radiation, indirectly ionizing such as neutrons and x-ray or gamma-ray photons, are not charged and cause ionization through a more complicated mechanism involving the emission

of energetic secondary charged particles which cause most of the ionization.

Directly ionizing radiation interacts very strongly with shielding media and is therefore easily stopped. By contrast, indirectly ionizing radiation, may be quite penetrating and the shielding required may be quite massive and expensive. For these reasons, nowadays much attention has been paid to the shielding of neutrons and photons, the two types of indirectly ionizing radiation most frequently encountered.

The main sources of radiation can be categorized as listed in Table 1.1.

Table 1.1: Main sources of radiation [2].

Category	Source/Machine	Radiation
Environmental	Cosmic Rays	Neutrons, protons, electrons, photons
	Radioactivity	α- and β- particles, γ-rays, neutrons
Artificial	Orthovoltage X-rays	kV X-rays
	Linac/betratron	MV X-rays, electrons and radioactivity
	Van de Graaff and Cyclotron	Protons, neutrons andradioactivity
	Synchrotron	Electrons, protons, X-rays, uv photons
	Nuclear Reactor	Neutrons, γ-rays, residual radioactivity

Along with understanding of the characteristics and potential benefits of different types of radiation came awareness of their potential harm. Thus from the need for protection was radiation shielding design and analysis born.

Radiation shielding serves a number of functions. Foremost among these is reducing the radiation exposure to persons in the vicinity of radiation sources. Shielding used for this purpose is named *biological shielding* [3]. Shields are also used in some reactors to reduce the intensity of γ-rays incident on the reactor vessel, which protects the vessel from excessive heating due to γ-ray absorption and reduces radiation damage due to neutrons. These shields are named *thermal shields* [3]. Sometimes shields are used to protect delicate electronic apparatus that otherwise would not function properly in a radiation shield. Such *apparatus shields* are used, for example, in some types of military equipment [3].

The basic radiation shielding process is illustrated in Figure 1.1:

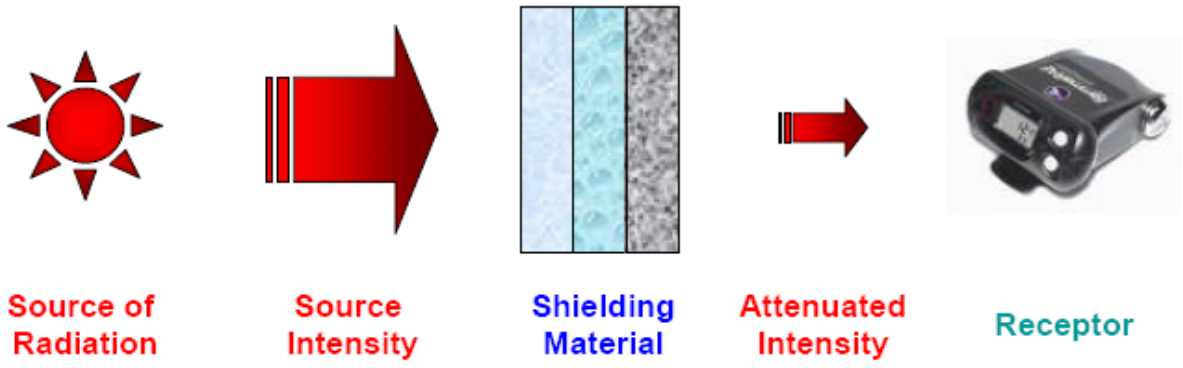

Figure 1.1: Basic radiation shielding process [4].

1.2 Radiation Shielding Materials

A variety of materials can be used for radiation shielding. To choose an appropriate type of shielding material, the type of radiation that is being shielded, the energy of the radiation, and the level of dose reduction are in need to be considered.

In choosing a shielding material, the first consideration must be effectiveness. If dealing with external radiation protection, the most important consideration must be personnel protection. An effective shield will cause a large energy loss in a relatively small penetration distance without emission of more hazardous radiation. However, other factors may also influence the choice of shielding materials such as, cost of the material, weight of the material, and how much space is available for the material. The effectiveness of the shielding material is determined by the interactions between the incident radiation and the atoms of the absorbing medium. The interactions which take place depend mainly upon the type of radiation, the energy of the radiation, and the atomic number of the absorbing medium. Among all the types of radiation, this work involved gamma-ray and neutron radiation.

Figure 1.2 shows some typical radiation shielding materials:

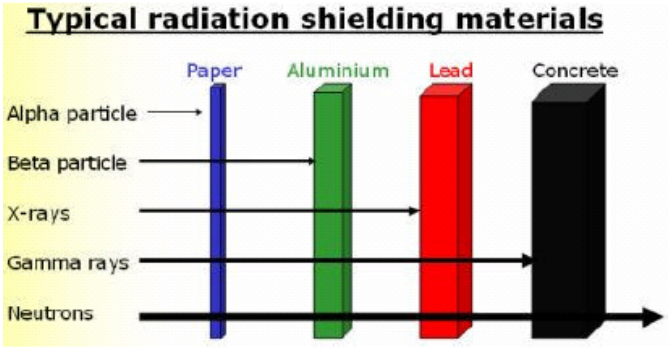

Figure 1.2: Typical radiation shielding materials [5].

1.2.1 Overview of Gamma-ray Shielding Materials

Gamma-rays are attenuated by processes which are functions of atomic number and mass (that is they all involve interactions near the nucleus or interactions with the electrons around the nucleus). Therefore, gamma radiation are best absorbed by atoms with heavy nuclei; the heavier the nucleus, the better the absorption [6].

Historically, materials with a high density and high atomic number are used to provide most effective gamma-ray shielding, such as lead, steel, tungsten, concrete and uranium. Some of them are listed:

- Lead: As one of the conventional gamma-ray shielding materials, lead is the most widely used material. Principally, lead is effective at attenuating gamma-rays because of its high density and high atomic number.

  Lead shields are frequently used where space is limited or where only a small area of absorber is required [7]. There is a great variety in the types of shielding available both to protect people and to shield equipment and experiments.

  Lead is widely used in the form of rectangular "lead bricks" in the construction of simple gamma-ray shields. A variety of lead shielding devices are available for laboratory equipment, including lead castles, structures composed of lead bricks, and thick containers for storing and transporting radioactive samples. Personal shielding includes lead aprons, thyroid shields, and lead gloves [8]. Lead and lead alloys have been used to some extent in nuclear reactor shields and have an added advantage of ease of fabrication. For some other commercially available shielding materials, a high percentage of lead can be incorporated into plastic or epoxy compositions, which can

be more readily molded and shaped [7]. However, because of its high ductility, lead cannot be machined easily or hold a given shape unless supported by a rigid material. Additionally, because of its low melting point, lead can be used only where the temperatures do not exceed its melting point.

- Iron or steel: It is also a common gamma-ray shielding material and is often used in situations where the size or configuration of the shield would make its construction from lead alone too expensive. In such circumstances, an outer layer of steel with inner lead lining is often an effective compromise [7].
- Tungsten: For small shields or collimators, tungsten is an attractive material consideration. It has shown that it can be effectively and economically utilized in large-scale applications and in shielding conditions that require a high degree of radiation attenuation in a limited thickness [7]. It possesses superior shielding factors compared to lead while removing the accompanying toxicity hazard and mixed waste processing costs. However, tungsten is over thirty times more expensive than lead; therefore, it is used sparingly and is almost never used for massive shields.
- Concrete: In situations where space is not a constraint and where structural strength is required, concrete is used even though it is a less effective shielding material. Concrete is often used in the construction of large-volume shields because of its low cost and most commonly used as the outer constituent of a shield, with its own activity shielded by an inner layer of steel, lead, or other shielding materials of lower activity [7].

- Depleted uranium and barium sulfate: They are also used in some special applications. When cost is important, almost any material can be used, but it must be far thicker. Most nuclear reactors use thick concrete shields to create a bioshield with a thin water cooled layer of lead on the inside to protect the porous concrete from the coolant inside [9].

Nowadays, some research work has been done with different types of glasses as a new gamma-ray shielding material. Gamma-ray shielding properties of various glasses have been studied theoretically and experimentally at different energies in literature [10-18, 27]. Examples are bismuth-borated glasses [12], ZnO-PbO-B_2O_3 glasses [14], CaO-SrO-B_2O_3 glasses [15], PbO-B_2O_3 glass system, Bi_2O_3-PbO-B_2O_3 glass systems [15], and PbO-BaO-B2O3 glass system [18], etc. It has been reported that compared with some standard radiation shielding concretes, these glasses have shown better performance in terms of their volume required for shield design with added advantage of being transparent to visible light [18].

1.2.2 Overview of Neutron Shielding Materials

The shielding of neutrons introduces many complications because of the wide range of energy that must be considered. Completely different principles apply to the selection of neutron shielding materials as compared with those for gamma rays. Whereas photon cross sections vary smoothly with atomic number and energy, neutron cross sections can change irregularly from element to element and have complicated resonance structures as functions of energy [19].Useful estimations are to be made by simple means in some circumstances,

while elaborate computer codes like Monte Carlo and other techniques could be employed to calculate neutron interactions and transport.

At low energies (less than 0.1 MeV), low atomic number materials, such as hydrogen in water, are best for slowing down neutrons. At these energies, the elastic cross section for interaction with hydrogen is high (approximately 20 barns), and the energy loss in a collision is high. Materials containing hydrogen are known as hydrogenous material, and their value as a neutron shield is determined by their hydrogen content.

- Water ranks high and is probably the best neutron shielding material with the advantage of low cost.
- Concrete, polyethylene and paraffin are also inexpensive sources of moderators.

For fast neutron (0.1-10 MeV) interactions, scattering becomes more important. The neutron can transfer an appreciable amount of energy in one collision. The secondary radiations in this case are recoil nuclei. At each scattering site, the neutron loses energy and is thereby moderated or slowed to lower energy.

Basically, fast neutrons need to be slowed down before being absorbed. A neutron shields acts to moderate fast neutrons to thermal energies, principally by elastic scattering, and then absorb them. Best materials for slowing down fast neutrons and increase their chances of absorption are lighter nuclei like hydrogen nuclei or protons, because neutrons exchange momentum and energy best with the particles of same size [20].

- The materials containing a lot of hydrogen per unit volume such as water, paraffin wax, and borated polyethylene (El-Khatib et al. 1996) have been used for absorbing fast neutrons.

Once the neutron has been moderated, it can be eliminated through an appropriate capture reaction. This absorption may be in the hydrogen already present for moderating purposes, although the capture cross section is relatively low. The thermal neutron may thus diffuse an appreciable distance before capture, reducing the effectiveness of the shield.

Furthermore, capture in hydrogen leads to the liberation of a 2.22 MeV capture gamma ray, which, because of its high energy, is particularly undesirable in many situations. Therefore, a second component is normally used in neutron shields, either homogenously mixed with the moderator or present as an absorbing layer. This additive is chosen to have a high neutron capture cross section, so that the moderated neutrons will preferentially undergo absorption within this material [7].

- Boron-10: The ^{10}B isotope has a high cross-section for absorption of thermal neutrons. This quality of good at capturing thermal neutrons has been used in both radiation shielding and in boron neutron capture therapy [21].

  In Pressurized Water Reactors (PWRs), it can serve either function in the form of borosilicate rods or boric acid. By adding more boric acid to the reactor coolant which circulates through the reactor, the probability that a neutron can survive to cause fission is reduced. Boron is also dissolved into the spent fuel pools containing used uranium rods. The concentration is high enough to keep fissions at a minimum [22].

  Additionally, in future manned interplanetary spacecraft, ^{10}B has a theoretical role as structural material (as boron fibers or BN nanotube material) which could serve a special role in neutron shielding [21]. The high energy spallation neutrons from the

secondary radiation can be moderated by materials high in light elements. Among light elements that absorb thermal neutron, ^{10}B appear as potential spacecraft structural materials able to do double duty in this regard [21].

- Cadmium and boron are generally used for thermal-neutron shielding because of their high thermal neutron absorption cross-sections. However, the yields of capture gamma-rays are also large, which are undesirable for medical and biological uses. To overcome this disadvantage, a novel neutron shielding material using a metathesis-polymer matrix has been developed in Japan. The ^{6}LiF metathene was shown to be practical and effective for medical and biological applications [23].

At higher energies (10 MeV), the cross section for interaction with hydrogen (1 barn) is not as effective in slowing down neutrons. If the energy of the fast neutron is sufficiently high, inelastic scattering with nuclei can take place in which the recoil nucleus is elevated to one of its excited states during the collision. The nucleus quickly de-excites, emitting a gamma-ray, and the neutron loses a greater fraction of its energy than it would in an equivalent elastic collision. Inelastic scattering and the subsequent gamma ray play an important role in the shielding of high-energy neutrons [23].

- Materials with good inelastic scattering properties, such as iron, are used to offset this decrease in cross section with increased neutron energy.
- Lead, which is generally used to provide shielding against gammas, has the added advantage of shielding against fast neutrons because of its high cross section for inelastic scattering when it is uniformly distributed throughout a hydrogenous material [9]. These materials can cause a large change in neutron energy after

collision for high energy neutrons but have little effect on the neutrons at lower energy, below 0.1 MeV [9].

1.2.3 Current Neutron-Gamma Radiation Shielding Materials

The rapid expansion of the nuclear industry requires shielding materials which not only must serve as an adequate shield but must also be available at a reasonable cost.

Among the conventional shielding materials, the most important shielding materials in use today include water, concrete, lead and iron. For an installation such as a nuclear reactor, both neutron and gamma radiation must be considered; combinations of several of these materials are therefore required for adequate protection. Some studies have already been carried out to seek for novel shielding materials with both the neutron and gamma-ray shielding ability. A number of them are briefly presented in this section.

Theoretically and experimentally, special glasses have been developed which accomplish the double task of allowing visibility while absorbing gamma-rays and neutrons, thus protecting the observer [25]. Glasses rich in boron and cadmium are used to absorb slow neutrons [26]. A number of these studies have been conducted in India.

In industry, a variety of neutron-gamma shielding materials have been developed and supplied by industry. Some examples are given here. Boronated rubber and other shielding rubber &polyethylene composite (e.g., lead-rubber & plastics composite) are produced in the Boron Rubbers India Company [28]; The composite neutron-gamma guard mixtures which have been proved the attributes/properties for potential applications in management of solid, liquid and sludge radioactive wastes, as well as mixed grout mixtures (WM'05 Conference,

February 27-March 3, 2005, Tucson, AZ). The Research/Experiment Polyethylene-based composites have been supplied by Reactor Experiments, Inc.

In some applications, given the additional need for weight reduction and practical considerations, there is a need for multifunctional materials which could perform structural or other roles while providing good radiation shielding capability. A kind of composite structure with boron phase and lead as the main elements has been designed in China. Characterization of this neutron-gamma shielding material and the methods to enhance strength and ductility of this integration structure is being studied [29].

1.3 Introduction to Metal Foams

"A metal foam is a cellular structure consisting of a solid metal-frequently aluminum, which contains a large volume fraction of gas-filled pores. The pores can be sealed (closed-cell foam), or they can form an interconnected network (open-cell foam). The defining characteristic of metal foams is a very high porosity: typically 75-95% of the volume consists of void spaces" [30].

Metal foam is a special class of porous materials with novel physical, mechanical, thermal, electrical and acoustic properties [31]. They exhibit a cellular structure with relatively low density and possess high strength, stiffness, high impact energy and sound absorption capacity, fire retardation and heat dissipation [32]. They are generally used in lightweight structural components and sandwich panels, in energy absorption systems for impact protection, as heat sinks for electronic devices, and as acoustic insulation [33, 34].

Among the most popular metals that have been foamed, the most popular are aluminum, iron, and titanium. Research has been done to develop metal foams made from carbon, copper, lead, tin, zinc, and titanium [35]. Additionally, foam has been developed using platinum and silver [36], silicon carbide [37], nickel [35, 38], molybdenum [39] and certain alloys such as iron-chrome, cobalt-chrome and nickel-copper [34].

Metal foams are made by a range of novel processing techniques, many still under development. The research into the manufacturing of these cellular metals has developed various techniques, which include: metal casting, powder metallurgy (PM), electro deposition, chemical vapor deposition (CVD) and physical vapor deposition (PVD) [40]. Generally, these methods developed to make metal foams fall into four classes: foam formed from the vapor phase, foam electrodeposited from an aqueous solution, foam from liquid-state processing and foam created from the solid state [43].

1.3.1 Properties of Metal Foams

Metal foams are characterized structurally by their cell topology, open cells or closed cells, relative density, cell size, cell shape and anisotropy. Important characteristic properties defining a metal foam includes its cell structure and relative density. Metal foams are either open cell, closed cell, or a combination of the two [42]. Closed-cell foam consists of a network of adjacent sealed pores, all sharing cell walls with each other. Because of this structure, fluids or gasses cannot pass through a closed-cell foam. Open-cell foam is made up of a network of interconnected solid struts, which allows the passage of a fluid or gas media. The type of cellular structure in a metal foam will give it different inherent characteristics. Figure 1.3 shows the close-ups of a closed-cell aluminum foam produced by

the Shinko Wire Company ((Figure 1.3 (a)) sand an open-cell aluminum foam produced by ERG Aerospace (Figure 1.3 (b)).

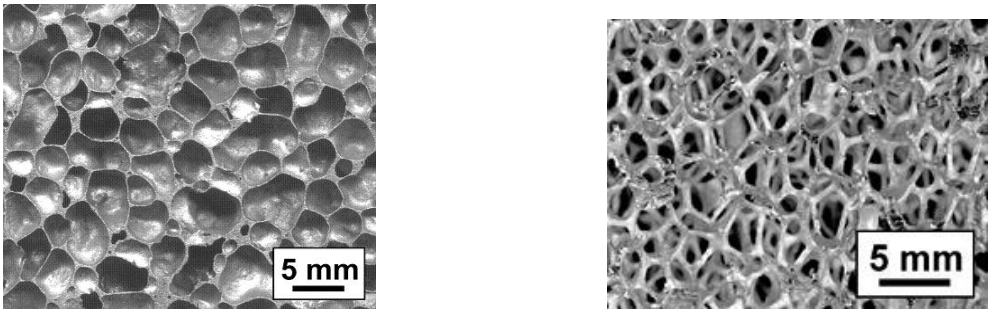

(a) (b)

Figure 1.3: Closed-cell aluminum foam (a) and open-cell aluminum foam (b) [30].

A metal foam has a pore density referred to as pores per inch (PPI). Lower pore density means the cell diameter for the pores will be larger compared to a sample with higher pore density. Fig. 1.4 shows three micrographs of 10, 20 and 40 PPI samples respectively.

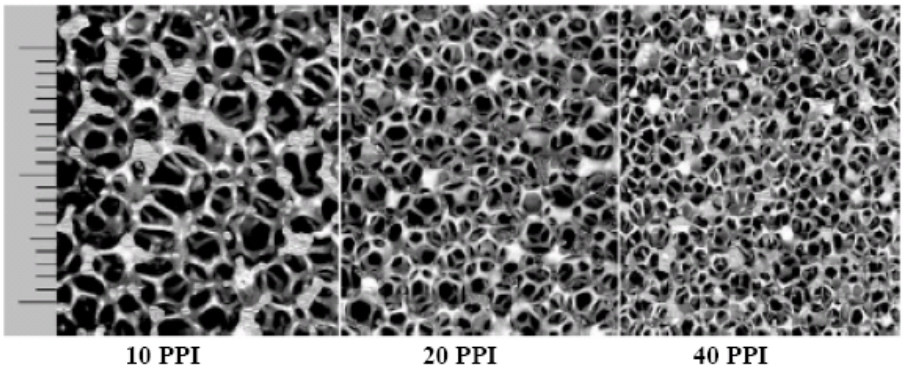

Figure 1.4: Samples of different pore density aluminum foam with a graduated millimeter scale [43].

Probably the most important parameter charactering a foamed material is its relative density. It is defined as the quantity $\rho/\rho_{s,}$ where ρ is the density of the cellular solid itself while ρ_s is the density of the material from which it is made [42]. Relative density directly

affects the cell size, cell wall thickness and pore diameter and consequently affects the mechanical and thermal properties of the foam [44].

Figure 1.5 shows a schematic of the typical stress-strain behavior of a metal foam under compressive loading [31]. This graph illustrates some of the defining mechanical properties. The densification strain point shown in the graph is the point at which the foam stops absorbing energy. It is the point at which the stress exceeds the plateau stress. The plateau stress level is defined as the average yield stress over the course of plastic deformation before densification. The Young's modulus is the ratio of stress to strain in the linear elastic region. In the elastic region, the metal foam displays cell wall bending. The area under the curve, up to the densification strain represents the energy absorbed by the material. In the densification region, the foam acts like solid metal.

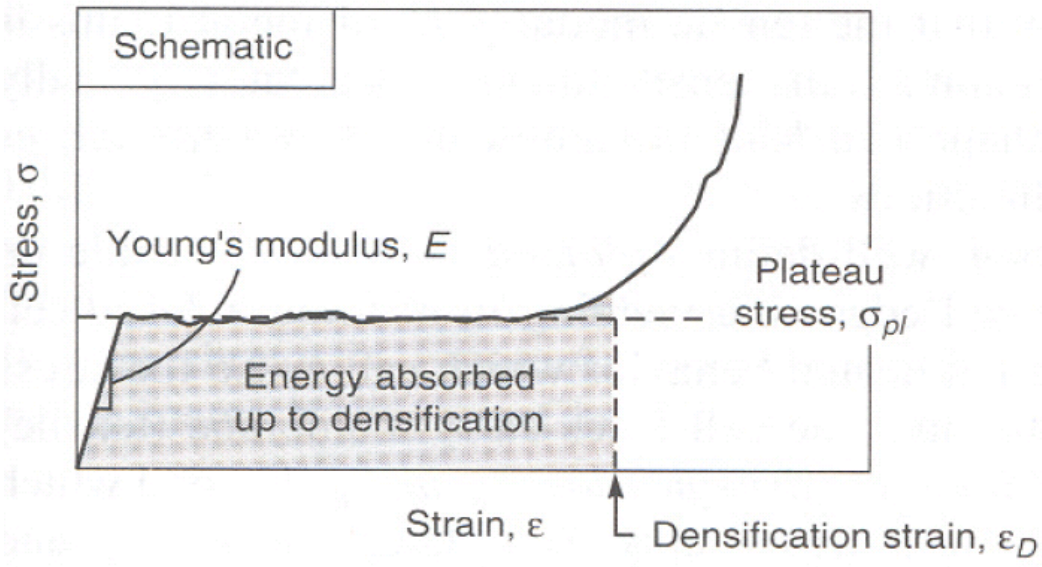

Figure 1.5: Compression curve for a metal foam – schematic showing properties [31].

Another mechanical property of metal foam that can be derived from the stress-strain curve is the impact energy absorption capacity [42]. This is defined as the area under the curve up to a certain strain. The defining value often quoted for metal foams is the energy absorbed at 50% strain [42]. Metal foams can deform plastically over a large region of strain while maintaining a low stress level, which may allow the metal foams' use in protecting objects to higher forces, such as automobiles in collisions.

The development of metal foams introduced improved properties when compared to non-metal foams and solid metals. In comparison to non-mental foams, metal foams exhibit higher stiffness, better strength to weight ratios, increased impact energy absorption, and a greater tolerance to high temperatures and adverse environmental conditions [41]. Compared to their solid material counterparts, metal foams offer higher specific stiffness (stiffness to weight ratio) [31]. By altering the size, shape and volume fraction of cells to engineer the mechanical properties, the demands of a wide range of specific applications can be met [31].

1.3.2 Applications of Metal Foams

The potential applications for metal foams have grown rapidly. A number of uses have been identified in industry in the fields such as aerospace engineering, machine construction, marine and rail transportation, automotive design, architectural and structural design and many additional functional applications [42]. The difference between the closed and open-cell configuration allows their different applications.

The pores in the open-cell metal foams allow the passage of fluids and gases. Open-cell metal foams have a wide variety of applications including heat exchangers, energy absorption, flow diffusion and lightweight optics. It is most typically used in advanced

technology aerospace and manufacturing [30]. Extremely fine-scale open-cell foams are used as high-temperature filters in the chemical industry [30]. For materials with a good resistance to oxidation and many forms of chemical attack such as aluminum, thus open-cell foams with small pore size can be used as high-temperature or chemically resistant filter materials. It has been suggested that liquid fuel containers could be partly filled with open-cell foams to prevent the flammable materials from spilling over a large area. Instead, they would at worst seep out gradually and burn on the surface of a block [48].

The combination of high electrical conductivity and a large surface area makes open-cell foams suitable for applications as electrodes, for example, in lead-acid batteries [48]. Open-cell foam structures are also useful as catalyst supports [31].

A very important application for open-cell metal foams is heat exchanger for airborne equipment, compact heat sinks for power electronics, heat shields, air-cooled condenser towers and regenerators (Antohe et al., 1996; Kaviany, 1985). The corrosion resistance, combined with a large surface area and a cell wall material with high thermal conductivity, makes open-cell foams ideal for use as heat exchanging materials [48]. Figure 1.6 shows two heat exchangers made of open-cell aluminum foam, courtesy of ERG Aerospace®. Figure 1.7 is a heat exchanger prototype manufactured by Porvair®.

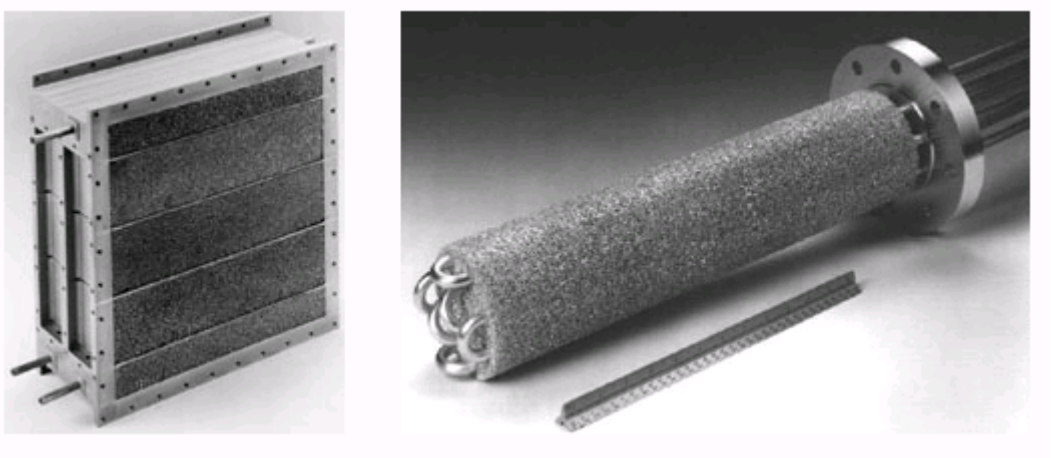

Figure 1.6: Two heat exchangers made of open-cell aluminum foam, courtesy of ERG Aerospace®.

Figure 1.7: A heat exchanger prototype made of open-cell foam, courtesy of Porvair®.

Research work in recent years has indicated that apart from low temperature applications such as compact heat exchangers for electronics cooling, open-cell metal foams can also be used in high-temperature applications such as the porous radiant burner and acoustic linear in combustors [45].

The thermal conductivities of closed-cell foams are, however, are lower than those of the fully dense parent metal by a factor of between 8 and 30 [31], due to the cellular structure. This makes them useful for some forms of thermal shielding.

Closed-cell foams are primarily used as an impact-absorbing material. They are light (typically 10-25% of the density of the metal they are made of, which is usually aluminum) and stiff, and are frequently proposed as a lightweight structural material.

The closed cell configuration is optimal for energy absorption and structural applications like in car bumpers, bridges and buildings. Figure 1.8 shows a sandwich panel made of close-cell foam core with steel sheets by Fraunhofer®, Germany for structurual applications.

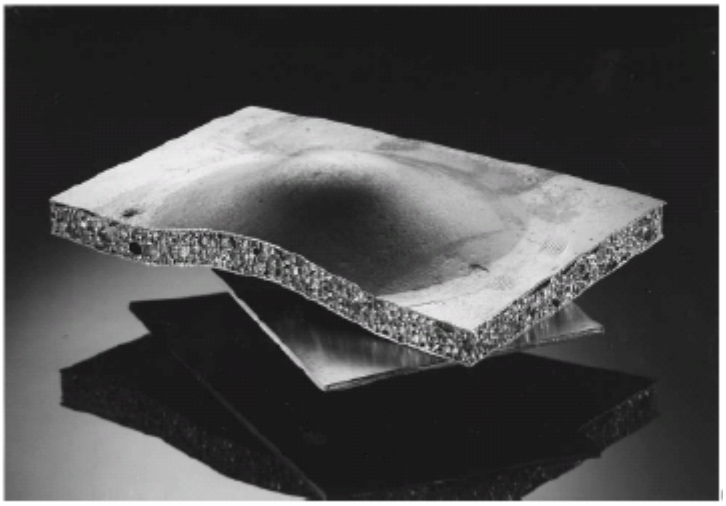

Figure 1.8: A sandwich panel with close-cell foam core, courtesy of Fraunhofer®.

Closed-cell foams have some applications in absorbing sound and damping vibration [42]. For example, Alporas® foams have been used as sound barriers on the underside of raised expressways in Japan [49]. It is initially closed-cell foam, but is rolled to have enough

deformation to crack some of the cell walls, in order to create pathways for sound waves to travel. In addition to noise attenuation, the material is fire resistant, weather resistant, and is non-toxic if exposed to flames [41].

A new type of closed-cell composite metal foam has been produced using a powder metallurgy technique [46]. Mechanical testing has indicated that the composite steel foams have superior energy absorbing capability and strength to density ratio. A more recent study on aluminum-steel composite metal foam processed by gravity casting technique has reported improved compressive and energy absorbing properties compared to those of other aluminum foams and steel hollow sphere foams [47]. The superior properties make these materials suitable for applications where the ability to deform at moderate stress levels and provide a high energy absorption capability is needed.

1.4 Metal Foams Used in this Work

The foam samples used in the experiments were the Duocel aluminum foams, which were the product of ERG Materials and Aerospace Corporation. Duocel foam is an open-celled structure with interconnected porosity. The base material of the foam samples is 6101 aluminum alloy and the relative density of samples is 8%.

The Duocel open-cell aluminum foams are fabricated from 6101 aluminum alloy using the so-called investment casting technique [32, 51]. A polymer foam is employed as a template, which is filled with a ceramic casting slurry. After baking to burn out the polymer foam template, a ceramic mould is created. Subsequently, the ceramic mould is infiltrated with a liquid aluminum alloy and after resolidification the ceramic is removed and an open-

cell aluminum alloy foam remains [52]. A consequence of this methodology is that the chemical composition of the 6101 aluminum foam differs from that of bulk 6101 aluminum [54], as shown in Table 1.3. Also the microstructure of the foam is different from that of the bulk alloy [52].

The Main physical properties of the Duocel foams used are listed in Table 1.2.

Table 1.2: Physical Characteristics of Duocel Aluminum Foam (8% Nominal density 6101-T6) [51].

Compression Strength	315 psi (2.17 MPa)
Tensile Strength	180 psi (1.24 MPa)
Shear Strength	190 psi (1.31 MPa)
Modulus of Elasticity (Compression)	$13.5 \cdot 10^3$ psi (93.08MPa)
Modulus of Elasticity (Tension)	$11 \cdot 10^3$ psi (75.84MPa)
Shear Modulus	$2.9 \cdot 10^4$ psi (199.95MPa)
Vickers Hardness	35
Specific Heat	.214 BTU·lb-1·°F-1 (.895 J·g-1·°C-1)
Bulk Thermal Conductivity	5.6 BTU·ft-1·hr-1·°F-1 (9.6 W·m-1·°C-1)
Coefficient of Thermal Expansion (0-100℃)	13.1 · 10-7·in·in-1·°F-1 (23.58 · 10-6·m·m-1·°C-1)
Bulk Resistivity	2.84 · 10-5 ohm · in (7.2 · 10-5 ohm · cm)
Melting Point	1220°F (660°C)

Table 1.3: Chemical composition (wt%) of bulk and foamed Al-6101 [52].

Samples	Cu	Mg	Mn	Si	Fe	Zn	B	Pb, Ni,Cr	Al
Bulk alloy	0.04	0.47	0.02	0.29	0.18	0.01	0.04	0.10 max	Balance
Foam	0.03	0.29	0.01	0.25	0.14	0.01	0.03	0.10 max	Balance

Samples of two pore sizes including 10 PPI and 20 PPI are used in these experiments, as shown in Figure 1.9.

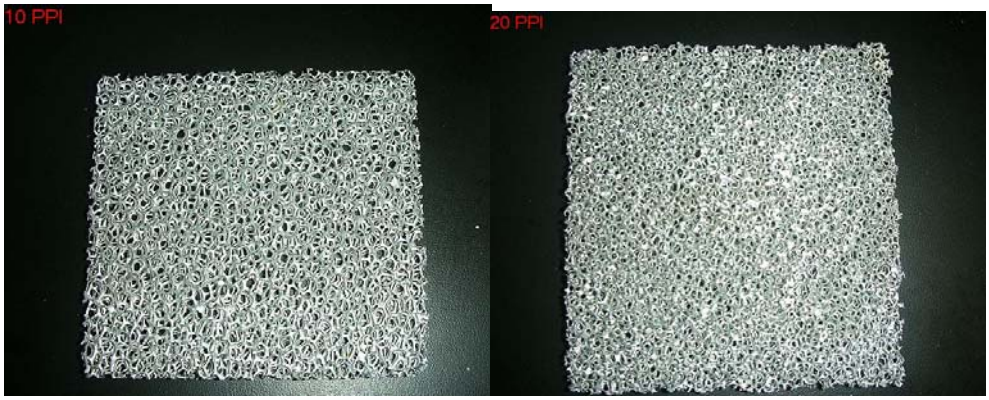

(a) (b)

Figure 1.9: 10 PPI (a) and 20 PPI (b) Duocel open-cell aluminum foam samples.

1.5 Purpose of the Present Work

As stated previously, there is a need to develop a new, efficient and lightweight structure, which can deal with not only one type of radiation and even carry out multifunctional tasks.

The objective of this work is to design an ultra-light structure using metal foams and investigate the structure's applicability of foams for radiation shielding in nuclear applications to meet the need.

The idea of this work is partly based on employing the porous nature of the metal foam which allows the relatively easy passage of fluid through it. By placing the foam samples in a plastic container, fluid is filled into it. And radiation attenuation measurements can be carried out with this structure. The attenuated intensity can be measured and results are to be compared between foam samples and bulk samples.

A number of advantages of this structure that can be imagined:

- Radiation shielding
- Weight saving
- Temperature control through water
- Mechanical strength

To validate the idea, this research tested and investigated the attenuation ability of this structure mainly based on experimental work. The structure in development is composed of layers of metals foams placed in a plastic container. The available resources used in this work are the cesium-137 and cobalt-60 radioactive sources from NCSU Nuclear Engineering Department for gamma-ray radiation, and the NCSU PULSTAR reactor as thermal neutron source. Gamma-ray transmission experiment and neutron transmission experiment were designed and set up. Multiple measurements were performed to determine the attenuation ability and the results were compared between the foam samples and bulk samples.

The first chapter gives an introduction to radiation shielding material and explains

why this research is needed. The second chapter provides the fundamental theories of this work. Chapter 4 describes all the design considerations, configuration details and measuring approaches about the experimental work. Chapter 4 provides experimental results, analyses and discussion. Chapter 5 includes summaries of this ongoing work and recommendations for future studies.

Chapter 2 Theory of Radiation Interactions

2.1 Interactions of Photons with Matter

2.1.1 Interaction Mechanisms

Unlike charged particles, photons are electrically neutral and do not steadily lose energy via columbic interactions with atomic electrons as do charged particles when they penetrate matter. Instead, they travel some considerable distance before interacting with an atom. All of the photon interactions of interest lead to partial or total transfer of the photon energy to electron energy. Thus the history of a photon in material is characterized by the sudden disappearance of the photon or by scattering through significant angles with significant energy loss.

Penetration of photons is governed statistically via interaction probabilities, which depends on the type of material of the specific medium traversed and on the photon energy. When the photon interacts, it might be absorbed and disappear or it might be scattered, changing its direction of travel, with or without loss of energy [55].

A photon interacts by one of the four following major processes. The probability of each is determined by a cross-section which depends on the photon energy and on the density and atomic number of the medium [4].

- Rayleigh (coherent) scattering: the photon interacts with the total electron cloud of an atom. Because the gamma-ray photon retains its original energy after the scattering event and virtually no energy is transferred, this process is often neglected in basic

discussion of gamma-ray interactions.

- Photoelectric absorption: the photon interacts with an inner atomic electron.
- Pair production: the photon converts into an electron-positron pair when it enters the strong Coulomb field surrounding an atomic nucleus.
- Compton (incoherent) scattering: the photon interacts with an individual electron whose binding energy is low compared to that of the incident photon.

The principal mechanisms of energy deposition by photons in matter are the last three types, which play an important role in radiation measurements and significantly influence the gamma-ray spectroscopy. The interaction can be the incident photon with the entire atom, as in the photoelectric absorption, or with one electron in the atom, as in the Compton scattering, or with the atomic nucleus (as in pair production). All these processes lead to the partial or complete transfer of the gamma-ray photon energy to electron energy. They result in sudden and abrupt changes in the gamma-ray photon history, in which the photon either disappear entirely or is scattered through a significant angle [7].

Photoelectric absorption predominates for relatively low-energy gamma-rays (up to several hundred keV, less than 0.5 MeV). In the photoelectric absorption process, a photon undergoes an interaction with an absorber atom in which the photon completely disappears. In its place, an energetic photoelectron is ejected by the atom from one of its boundary shells. The interaction is with the atom as a whole and cannot take place with free electrons.

The energy-transfer is a two-step process. The photoelectric interaction in which the photon transfers its energy to the electron is the first step. The deposition of the energy in the surrounding matter by the electron is the second step. For gamma rays with sufficient energy,

the most probable origin of the photoelectron is the most tightly bound or K shell of the atom. The photoelectron appears with an energy given by:

$$E_{e^-} = h\nu - E_b \tag{2.1}$$

where E_b represents the binding energy of the photoelectron in its original shell. Hence for gamma-ray energies of more than a few hundred keV, the photoelectron carries off the majority of the original photon energy.

The photoelectric process is enhanced for absorber materials of high atomic number Z. A rough approximation for the probability of photoelectric absorption (τ) per atom over all ranges of E_γ and Z is [7]:

$$\tau \cong \text{constant} \times \frac{Z^n}{E_\gamma^{3.5}} \tag{2.2}$$

where the exponent n varies between 4 and 5 over the gamma-ray energy region of interest. This severe dependence of the photoelectric absorption probability on the atomic number of the absorber is a primary reason for the preponderance of high-Z materials (such as lead) in gamma-ray shields.

The photoelectric interaction is most likely to occur in the occasion that the energy of the incident photon is just greater than the binding energy of the electron it interacts with. For this reason, the plot of the attenuation coefficient as a function of the photon energy is a complicated relationship, with sharp peaks at the binding energies of the various orbital shells and with strong dependence on the atomic number of the atom [56]. Figure 2.1 is a log-log plot of the photoelectron interaction probability vs. energy. In the plot, the K and L orbital edges for lead are visible, while K and L binding energies for water are not visible.

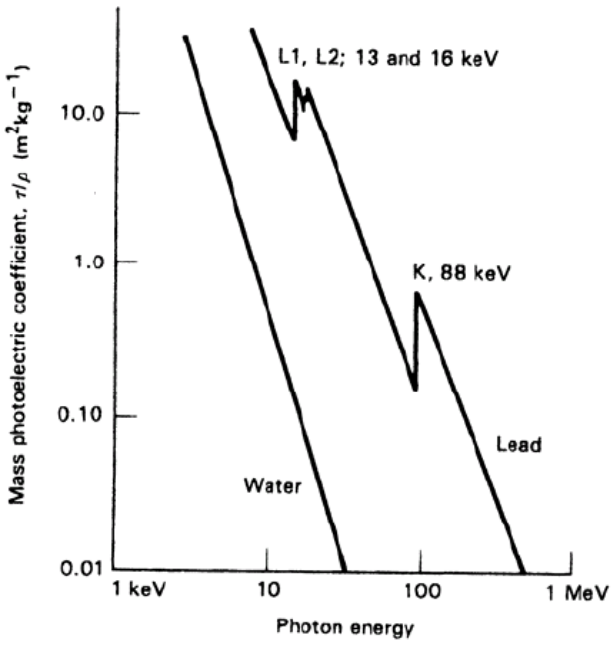

Figure 2.1: Plot of photoelectric mass attenuation coefficient as a function of photon energy for water and lead [56].

Pair production predominates for high-energy gamma-rays (higher than 1.022 MeV). In the interaction which must take place in the coulomb field of a nucleus, the gamma-ray disappears and reappears as an electron-positron pair. All the excess energy, carried in by the photon above the 1.022 MeV as required to create the pair, goes into kinetic energy shared by the positron and electron. The positron will subsequently annihilate after slowing down in the absorbing medium. As a result, two annihilation photons are normally produced as secondary products of the interaction.

The probability of pair production increases with increasing photon energy, and it usually increases with atomic number approximately as Z^2 [56].

Compton scattering is the most probable process over the range of energies between these extremes (0.5-5.0 MeV). A Compton interaction is one in which only a portion of the energy is absorbed and a photon is produced with reduced energy. The interaction process takes place between the incident gamma-ray photon and an electron in the absorbing material. It is often the predominant interaction mechanism for gamma-ray energies typical of radioisotope sources [7].

In Compton scattering, the incoming gamma-ray photon is deflected through an angle θ with respect to its original direction. The photon transfer a portion of its energy to the electron (assumed to be initially at rest), which is then known as a *recoil electron*. The energy transferred to the electron can vary from zero to a large fraction of the gamma-ray energy, for the reason that all angles of scattering are possible.

For low-energy photons, little energy is transferred when the scattering takes place, regardless of the probability of such an interaction. As the energy increases, the fractional transfer increases, approaching 1.0 for photons at energies above 10 to 20 MeV [56].

The probability of Compton scattering per atom of the absorber depends on the number of electrons available as scattering targets and therefore increases linearly with Z.

The relative importance of the three processes described above for different absorber materials and gamma-ray energies is illustrated in Figure 2.2. The left and right lines represent the energy at which photoelectric absorption and Compton scattering, Compton scattering and pair production are equally probable as a function of the absorber atomic number, respectively. Three areas are then defined on the plot within which the three types of interaction predominate.

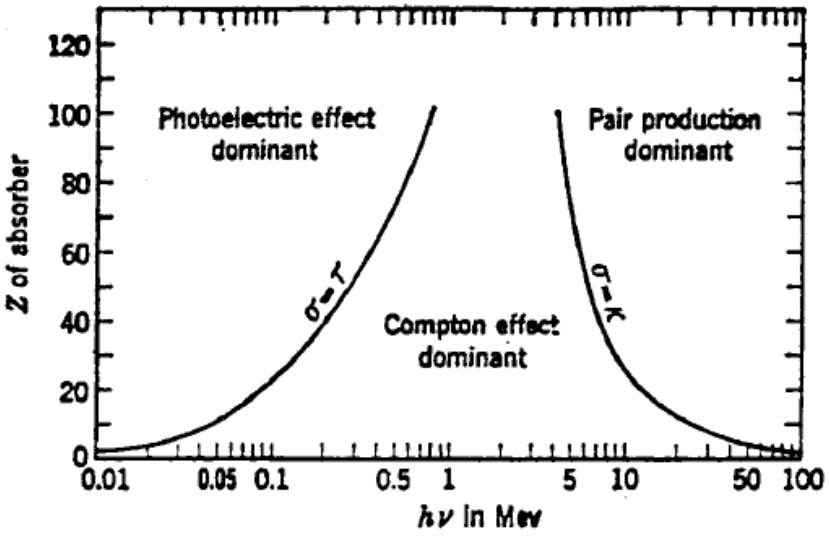

Figure 2.2: The relative importance of the three major types of gamma-ray interaction [57].

2.1.2 Attenuation Coefficients

The Fundamental Law of Gamma-ray Attenuation

Figure 2.3 illustrates a simplified transmission experiment, where monoenergetic gamma-rays are collimated into a narrow beam and allowed to strike a detector after passing through an absorber of variable thickness.

When a gamma ray passes through matter, the probability for absorption in a thin layer is proportional to the thickness of that layer. This leads to an exponential decrease of intensity with thickness. It should be noted here that the exponential absorption holds only for a narrow beam of gamma-rays. If a wide beam of gamma-rays passes through a thick slab of concrete, the scattering from the sides reduces the absorption.

A parallel beam of monoenergetic gamma photons is attenuated in matter according to the Lamber-Bee law, which is given by the exponential expression:

$$I = I_0 \exp(-\mu t) \tag{2.3}$$

where I_0 and I are the incident and transmitted intensities, t is the thickness of the absorbing medium and μ is the linear attenuation coefficient.

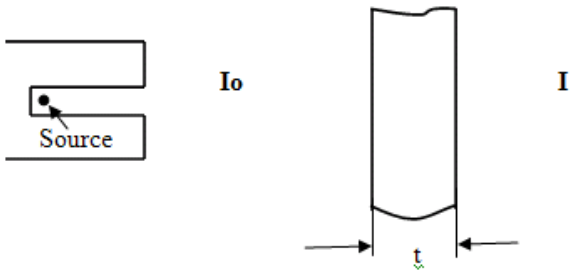

Figure 2.3: A simplified transmission experiment.

Equation (2.3) is a description of the gamma-ray attenuation experiment in which the gamma-rays are collimated to a narrow beam before striking the absorber, sometimes characterized as a "narrow beam" or "good beam geometry" measurement. The essential characteristic is that only gamma-rays from the source that escape interaction in the absorber can be counted by the detector. Real measurements are often carried out under different circumstances in which the sever collimation of the gamma-rays is absent. The conditions that lead to the simple exponential attenuation of equation (2.3) are therefore violated in this "broad beam" or "bad geometry" measurement [7]. Therefore the buildup factor is introduced to modify this equation. In this work, in order not to complicate this situation, a good narrow beam geometry was established and the buildup factor was ignored in the calculation, which will be talked about in details in Chapter 3.

Linear Attenuation Coefficient

Each of the interaction processes described before removes the gamma-ray photon from the beam either by absorption or by scattering away from the detector direction and can be characterized by a fixed probability of occurrence per unit path length in the absorber. The sum of these probabilities is simply the probability per unit path length that the gamma-ray photon is removed from the beam [7]:

$$\mu=\tau \text{ (photoelectric)} + \sigma \text{ (Compton)} + \kappa \text{ (pair)} \tag{2.4}$$

and is called the *linear attenuation coefficient* (or *macroscopic cross-section*), which has the dimensions of inverse length (e.g., cm^{-1}). The number of transmitted photons I is then given in terms of the number without an absorber I_0 as:

$$\frac{I}{I_0} = e^{-\mu t} \tag{2.5}$$

The ratio I/I_0 is called the gamma-ray transmission (T), which is a function of gamma-ray energy, absorber composition, and absorber thickness.

The linear attenuation coefficient, also called the *narrow beam attenuation coefficient*, is a quantity which describes the extent to which the intensity of energy beam is reduced as it passes through a specific material. As measurements with different sources and absorbers have shown, the linear attenuation coefficient depends on the gamma-ray energy and the atomic number and density of the absorber. Generally, the higher the energy of the incident photons and the less dense the material in question, the lower the corresponding linear attenuation coefficient will be. Figure 2.4 illustrates exponential attenuation for three different gamma-ray energies and shows that the transmission increases with increasing

gamma-ray energy and decreases with increasing absorber thickness.

Figure 2.5 is a description of the linear attenuation coefficient of aluminum for gamma-rays, plotted versus gamma energy, and the contributions by the three effects. Over most of the energy region shown, the Compton Effect dominates. Figure 2.6 is a description of the linear attenuation coefficient of lead. For lead, the photo effect dominates at low energy. Above 5 MeV, pair production starts to dominate.

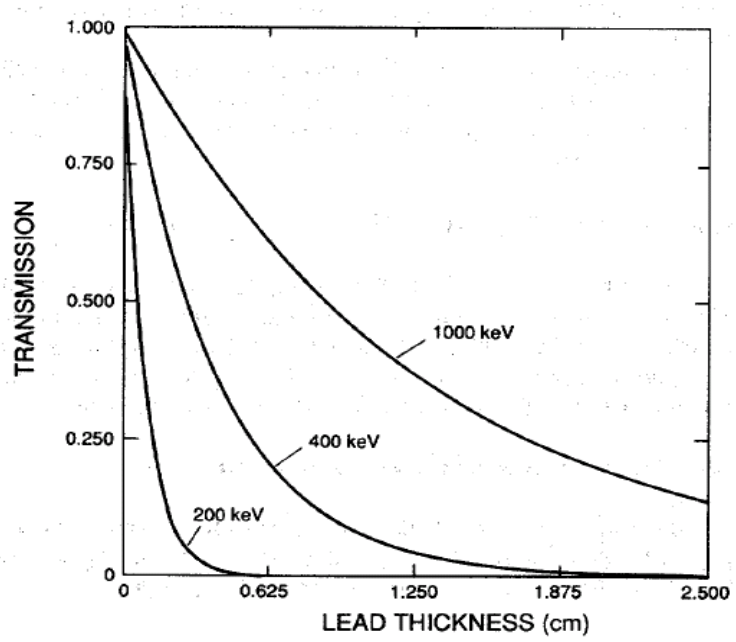

Figure 2.4: Transmission of gamma-rays through lead absorbers [58].

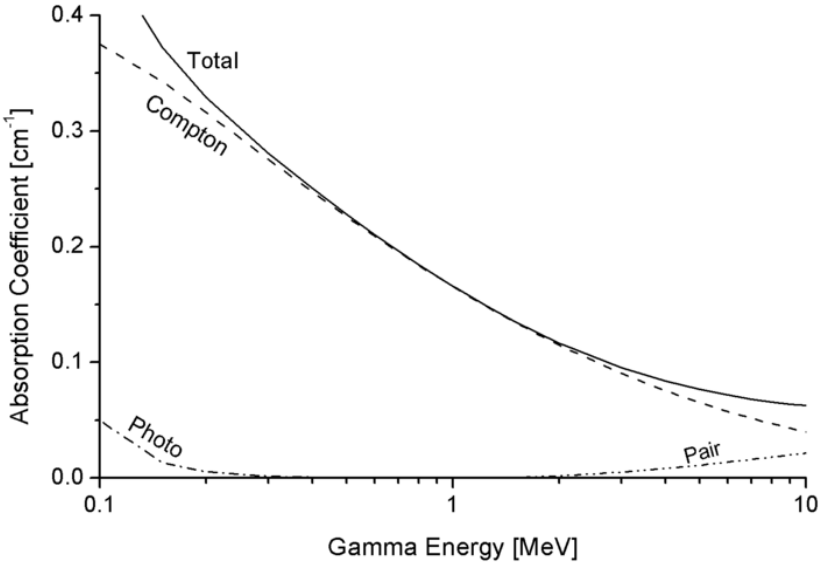

Figure 2.5: The total linear attenuation coefficient of aluminum for gamma-rays [50].

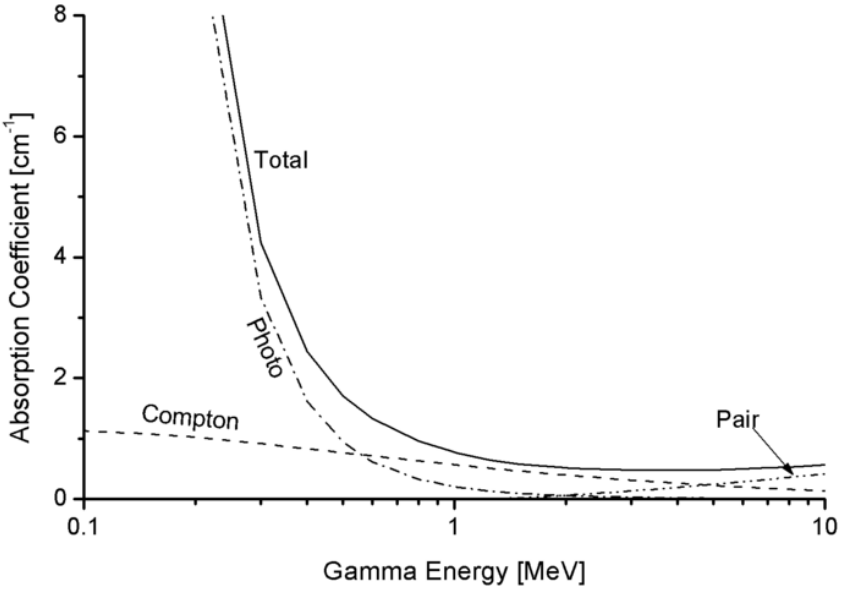

Figure 2.6: The total linear attenuation coefficient of lead for gamma-rays [50].

Alpha and beta particles have a well-defined range of stoPPIng distance. But as Figure 2.4 shows, gamma-rays do not have a unique range. The reciprocal of the linear attenuation coefficient, $1/\mu$, has units length and often called the mean free path λ. For photons in an attenuating medium, λ is defined as the average distance a gamma-ray travels in the absorber before interacting [6]; it is also the absorber thickness that produces a transmission of 1/e, or 0.37. Typical values of λ are in the range from a few mm up to tens of cm in solids for common gamma-ray energies.

Mass Attenuation Coefficient

The linear attenuation coefficient is the simplest absorption coefficient to measure experimentally, but it is not usually tabulated because of its dependence of the absorbing material. For example, at a given energy, the linear coefficients of water, ice and steam are all different, even though the same material is involved.

The fact that the linear attenuation coefficient varies with the density of the absorber limits its use, even if the absorber material is the same. Therefore, the mass attenuation coefficient is much more widely used and is defined as:

$$\text{mass attenuation coefficient} = \frac{\mu}{\rho} \tag{2.8}$$

where ρ represents the density of the absorbing medium. It has the dimensions of area per unit mass (cm^2/g). Mass attenuation coefficient values are actually normalized with respect to material density, and do not change with changes in density. For a given gamma-ray energy, the mass attenuation coefficient does not change with the physical state of a given absorber. For the example mentioned above, it is the same for water whether present in liquid or vapor

form.

The mass attenuation coefficient of a chemical compound or mixture can be calculated from:

$$\frac{\mu}{\rho} = \sum_i w_i (\frac{\mu_i}{\rho_i}) \tag{2.9}$$

where w_i is the weight fraction of element i in the compound or mixture.

The values of mass attenuation coefficients are dependent upon the absorption and scattering of the incident radiation cause by several different mechanisms, such as Rayleigh (coherent) scattering, Compton (incoherent scattering), Photoelectric Absorption, and Pair Production.

The major three interaction processes described all contribute to the total mass attenuation coefficient. The relative importance of the three interactions depends on gamma-ray energy and the atomic number of the absorber. Figure 2.7 shows a composite of mass attenuation curves covering a wide range of energy and atomic number. The interplay of the three processes is shown dramatically. All elements except hydrogen show a sharp, low-energy rise that indicates where photoelectric absorption is the dominant interaction [58]. The position of the rise is very dependent upon atomic number. Above the low-energy rise, the value of the mass attenuation coefficient decreases gradually, indicating the region where Compton scattering dominates. The mass attenuation coefficients for all elements with atomic number less than 25 (iron) are nearly identical in the energy range 200 to 2000 keV. The attenuation curves of hydrogen shows it interacts with gamma-rays with energy greater than 10 keV almost exclusively by Compton scattering. Above 2 MeV, the pair production

becomes important for high-Z elements and the mass attenuation coefficients begin to rise again.

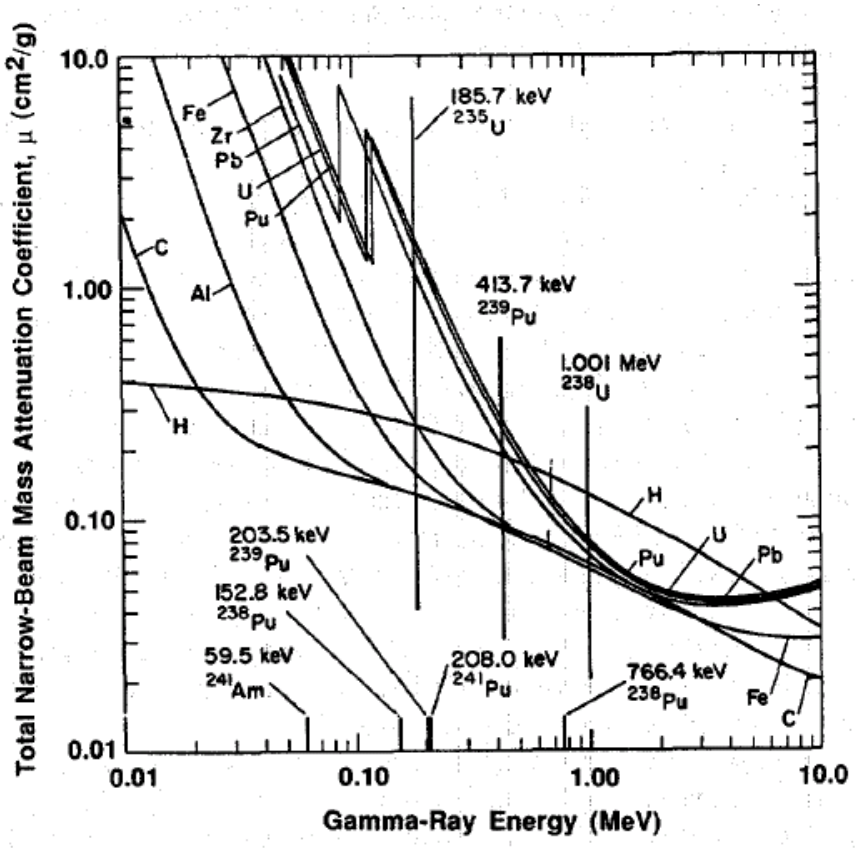

Figure2.7: Mass attenuation coefficients of selected elements [58].

The actually values have been thoroughly examined and are available to general public through three databases run by National Institute of Standards and Technology (NIST) [50]:

- XAAMDI database
- XCOM database
- FFAST database

2.2 Interactions of Neutrons with Matter

Cross-sections

The design of radiation shielding depends fundamentally on the way in which nuclear radiation interacts with matter. Since neutrons are electrically neutral, they are not affected by the electrons in an atom or by the positive charge of the nucleus. As a consequence, neutrons pass through the atomic electron cloud and interact directly with the nucleus.

Neutrons may interact with nuclei in one or more of the following ways [7]:

- Elastic scattering (n, n) reaction
- Inelastic scattering (n, n') reaction
- Radiative Capture (n, γ) reaction
- Charged-particle reactions (n, α) or (n, p) reaction
- Neutron-producing reactions (n, 2n) or (n, 3n) reaction
- Fission

The interactions of neutrons with nuclei are divided into two categories: scattering and absorption.

In scattering interactions, the neutron interacts with a nucleus, but both particles reappear after the reaction. A scattering collision is indicated as an (n, n) reaction or as:

$$n + {}^{A}_{Z}X \rightarrow + {}^{A}_{Z}X + n$$

Scattering may be elastic or inelastic. In elastic scattering, the total kinetic energy of the two colliding particles is conserved. In inelastic scattering, part of the kinetic energy is given to the nucleus as excitation energy. The excited nucleus will decay and return to the ground state by emitting gamma-rays.

In an absorption reaction, the neutron disappears, but one or more other particles appear after the reaction takes place. Table 2.1 lists some examples of absorptive reactions.

Table 2.1: Absorption Reactions.

Reaction	Name
$n + {}^{A}_{Z}X \rightarrow {}^{A}_{Z-1}Y + p$	(n, p) reaction
$n + {}^{A}_{Z}X \rightarrow {}^{A-3}_{Z-2}Y + {}^{4}_{2}He$	(n, α) reaction
$n + {}^{A}_{Z}X \rightarrow {}^{A-1}_{Z}Y + 2n$	(n, 2n) reaction
$n + {}^{A}_{Z}X \rightarrow {}^{A+1}_{Z}Y + \gamma$	(n, γ) reaction
$n + {}^{A}_{Z}X \rightarrow {}^{A_1}_{Z_2}Y_1 + {}^{A_2}_{Z_2}Y_2 + n + n + \ldots$	reaction

The extent to which neutrons interact with nuclei is described in terms of quantities known as *cross-sections*. Neutron cross-sections depend strongly on the energy of the neutron as well as on the atomic weight and atomic number of the target nucleus.

Consider a monoenergetic parallel beam of neutrons hitting a thin target of thickness t and area A as shown in Figure 2.8. The number of reactions per second, R, taking place in this target could be written as

R (reactions / s) = (neutrons per m^2 s hitting the target) (targets exposed to the beam)

× (probability of interaction per n/m^2 per nucleus) (2.10)

or

$$R = I\,[n/(m^2\,s)]\,[N\,(\text{nuclei}/m^3)]\,[a\,(m^2)]\,[t\,(m)]\,[\sigma\,(m^2)] \quad (2.11)$$

where I, a, and t are shown in Figure 2.8. The parameter σ, called the cross section, has the

following physical meaning:

σ (m^2) = probability that an interaction will occur per target nucleus per neutron per m^2 hitting the target.

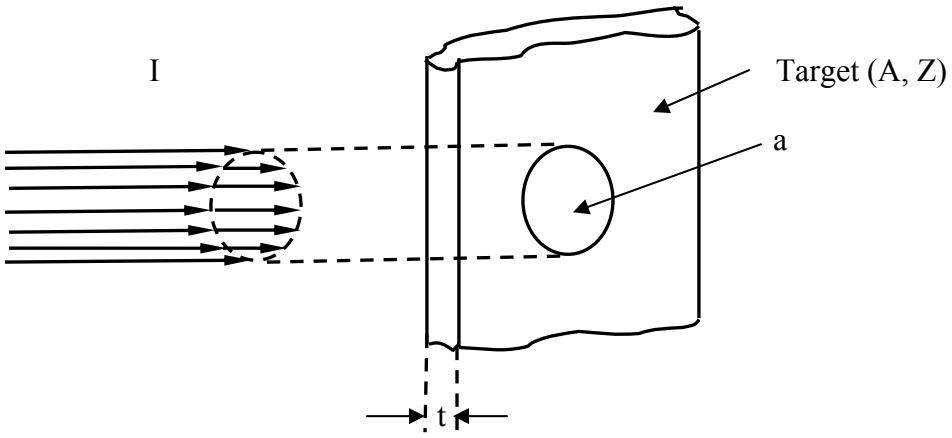

Figure 2.8: A parallel neutron beam hitting a thin target, a = area of target struck by the beam.

Neutron cross-sections are defined separately for each type of reaction and isotope as following:

σ_e = elastic scattering cross section

σ_i = inelastic scattering cross section

σ_a = absorption cross section

σ_γ = capture cross section

σ_f = fission cross section

The total cross-section, which measures the probability that an interaction of any type will occur when neutrons strike a target, equals the sum of all cross-sections:

$$\sigma_t = \sigma_e + \sigma_i + \sigma_\gamma + \sigma_f + ... \tag{2.12}$$

In the notation used here, the sum of the cross-sections of all absorption reactions is known as the absorption cross-section and is denoted by σ_a.

$$\sigma_a = \sigma_\gamma + \sigma_f + \sigma_p + \sigma_\alpha + ... \tag{2.13}$$

where σ_p and σ_α are the cross-sections for the (n, p) and (n, α) reactions respectively. Similarly, the total scattering cross-sections is the sum of the elastic and inelastic scattering cross-sections. Thus,

$$\sigma_s = \sigma_e + \sigma_i \tag{2.14}$$

and

$$\sigma_t = \sigma_s + \sigma_a \tag{2.15}$$

The total microscopic cross-section σ_t (b) of a material means its unique capability of removing neutrons, especially thermal ones, from their tracks. Another form of the cross section, also frequently used, is the macroscopic cross section $\sum$ (m-1). In particular, the product $N\sigma_t = \sum_t$ is called the macroscopic total cross-section, where the number of nuclei N per unit volume is the atom density with unit of cm^{-3}. This quantity has the same significance for neutrons as the linear absorption coefficient for gamma rays defined earlier. If a narrow beam attenuation experiment is carried out for neutrons, as sketched earlier for gamma rays, the results will be the same: The number of detected neutrons will fall off exponentially with absorber thickness. In this case the attenuation relation is written as:

$$\frac{I}{I_0} = e^{-\sum_t t} \tag{2.16}$$

Thus, the fundamental equation for the thermal neutron transmission measurements in this work is:

$$I = I_0 * \exp(-\sigma_t * N * t) = I_0 * \exp(-\sum_t * t) \quad (2.17)$$

The neutron mean free path λ is, by analogy with the gamma-ray case, given by $1/\sum_t$. In solid materials, λ for slow neutrons may be of the order of a centimeter or less, whereas for fast neutrons, it is normally tens of centimeters.

Figure 2.9 shows a simplified experimental arrangement for a transmission experiment. If Z_0 is the counting rate at the detector with no sample, then after insertion of a sample of thickness d the counting rate is:

$$Z = Z_0 * \exp(-\sigma_t N d) \quad (2.18)$$

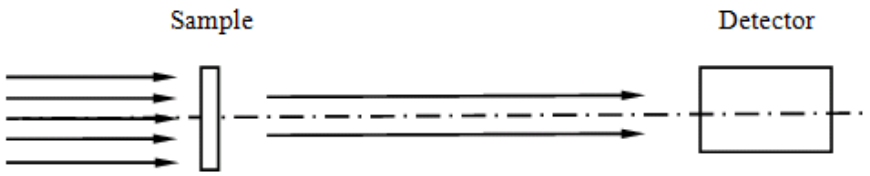

Figure 2.9: Principle of a transmission experiment.

If $T=Z/Z_0$ is defined as the transmission of the sample, the total cross section σt can be expressed as [59]:

$$\sigma_t = \frac{1}{Nd} \ln \frac{1}{T} \quad (2.19)$$

Under most circumstances, neutrons are not narrowly collimated so that typical shielding situations involve broad beam or "bad geometry" conditions. Then the exponential attenuation of Equation (2.17) is no longer an adequate description because of the added importance of scattered neutrons reaching the detector. The configuration of a "good geometry" is described in the following chapter.

Ch 3 Experimental

3.1 Overall Design

Taking into count the availability for gamma-ray and neutron radiation sources, the experimental work was designed and carried out in the following way:

- Gamma-ray transmission experiment
- Thermal neutron transmission experiment

In both the experiments, the source, the absorber, and the detector were arranged along a straight line. The foam samples used in these experiments were open-cell foams which could be filled with fluid through the cells. Measurements were conducted with bulk material samples, foam samples, and foam samples filled with liquid. In each measurement, samples were placed in a plastic container which helped hold the samples. And the design of the structure was different in order to adjust to different configurations.

In the gamma-ray experiment, the Cs-137 source of photon energy 0.662 MeV and Co-60 source of photon energy 1.173 MeV and 1.332 MeV were used for gamma-ray emission. To set up this transmission geometry, a steel stand was made to hold the detector and its surrounded lead shielding. A vertical arrangement was established and well aligned. This design is illustrated as in Figure 3.1.

In the neutron experiment, a horizontal beam emitted from NCSU PULSTAR reactor beam port #5 was utilized as thermal neutron source. A transmission geometry was set up and aligned. The bottom plastic sheet of the container has a few grooves so that a plastic

sheet could be flexibly inserted into the grooves and moved between the grooves, in order to adjust with different layers of foam samples. This design is shown in Figure 3.2.

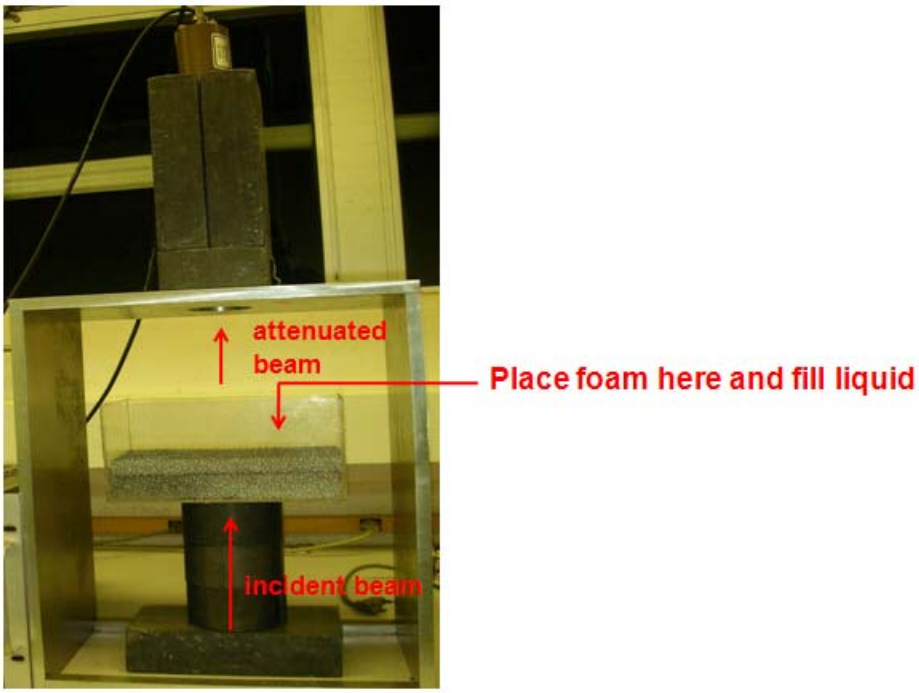

Figure 3.1: Design of gamma-ray transmission experiment.

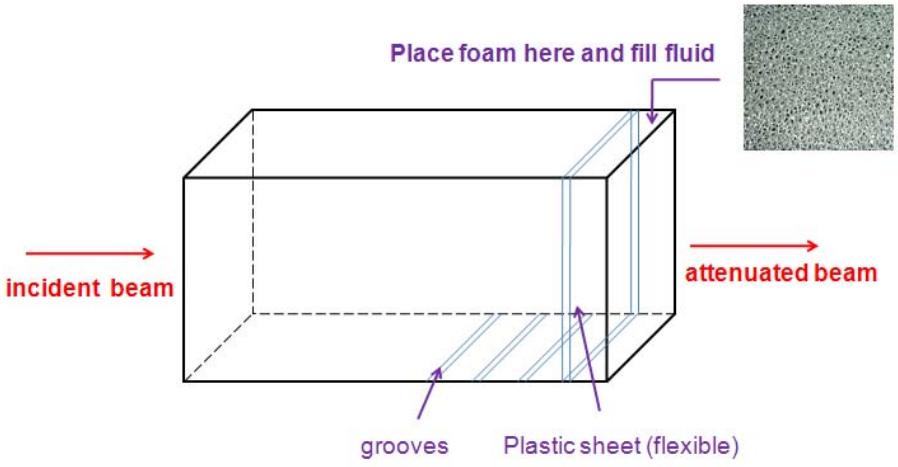

Figure 3.2: Design of neutron transmission experiment.

3.2 Gamma-ray Attenuation Measurements

3.2.1 Sources and Sample preparation

The radioactive sources of Cs-137 and Co-60, each with the strength of 2 mCi and 1.2 mCi, were obtained from Nuclear Engineering Department at North Carolina State University. Both sources were housed in a lead container during measurements.

The samples used in gamma-ray attenuation measurements were bulk pure aluminum, bulk aluminum 6061 alloy, aluminum foams made from bulk aluminum 6101 alloy.

The samples were cut to a couple of slabs in the machine shop in Mechanical & Aerospace Department at North Carolina State University, to obtain certain different thicknesses for better comparisons of experimental results.

Dimensions and quantities of all the samples with different materials are listed in Table 3.1.

Table 3.1: Samples used in gamma-ray attenuation measurements.

Samples	Dimensions (inch)	Quantity (piece)
Bulk pure Al	4×3.75×0.25	6
Bulk Al 6061 alloy	4×3.75×0.25	3
10PPI Al foam	4×3.75×0.5	2
	4×3.75×0.75	2
20PPI Al foam	4×3.75×0.5	4
	4×3.75×0.75	1

3.2.2 Counting Electronics

The counting electronics used in the gamma-ray experiment is shown as a circuit in Figure 3.3.

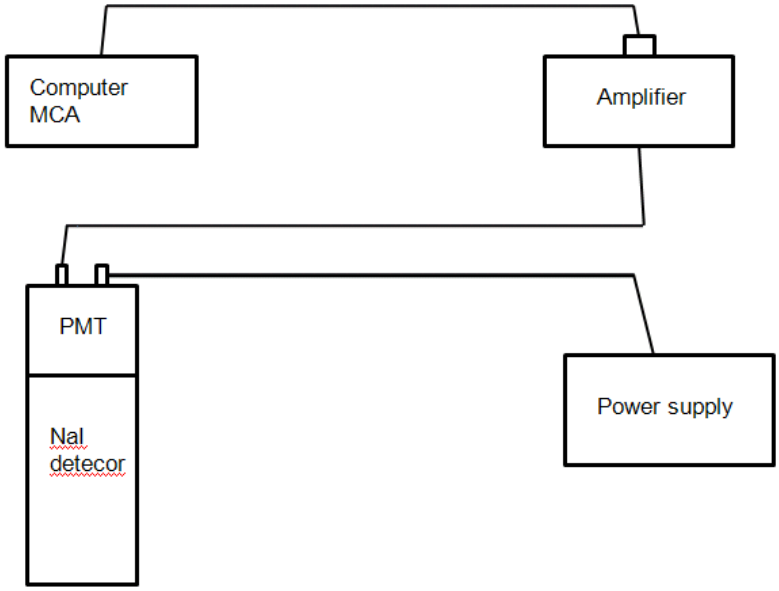

Figure 3.3: Schematic of electronics in gamma-ray experiment.

The electronics used:

- Detector: ORTEC Sodium Iodide (NaI) Detector (Model 905-3, 2"×2") with Photomultiplier Tube (PMT) base (Model 266)
- Amplifier: ORTEC Model 485
- Bin: ORTEC Model 401A
- High Voltage Power Supply: Ortec Model 556

  Operating voltage: 700 kV

Here, the NaI detector is a 2×2 inch cylindrical scintillation detector. The detector system begins with a crystal of Sodium Iodide, where gamma-rays will interact with the iodine with a sufficiently high cross section. The crystal is located next to a photomultiplier tube (PMT) and the scintillator/PMT (detector) is enclosed in a reflective, light-tight housing. The PMT consists of a photocathode, a focusing electrode, and 10 or more dynodes that multiply the number of electrons striking at each dynode. A chain of resistors (not shown) typically located in a plug-in tube base assembly biases the anode and dynodes. Scintillation photons striking the photocathode eject electrons via the photoelectric effect. A high voltage (HV) power supply and the resistor chain bias the cathode, dynodes, and anode so as to accelerate electrons from the cathode into the first dynode, from one dynode to the next, and from the final dynode to the anode collector. Each incident electron strikes a dynode with enough energy to eject around 5-10 (secondary) electrons from that dynode. For each initial photoelectron, by the end of that chain, there are on the order of 10^6 electrons reaching the anode. From this process, a gamma-ray interacting with a scintillator produces a pulse of light that is converted to an electric pulse by a photomultiplier tube. After the electrical pulses are converted to voltage pulses through an amplifier, these pulses are then sorted by height, counted and stored in the multichannel analyzer which displays the resulting spectrum.

Because the amount of number of photons produced in the scintillation crystal is proportional to the amount of gamma-ray energy initially absorbed in the crystal, so are the number of photoelectrons from the cathode, the final anode charge, and the amplitude of the amplifier voltage pulses. The overall effect is that the final pulse height is proportional to gamma energy absorbed in crystal.

3.2.3 Data Acquisition Method

The Canberra Genie 2000 Gamma Acquisition & Analysis was used as the software platform for the transmitted gamma spectroscopy acquisition.

Genie 2000 is a comprehensive set of capabilities for acquiring and analyzing spectra from Multichannel Analyzers (MCAs).Its functions include MCA control, spectral display and manipulation, basic spectrum analysis and reporting [59].

A block diagram of the Genie 2000 architecture is shown in Figure 3.4.

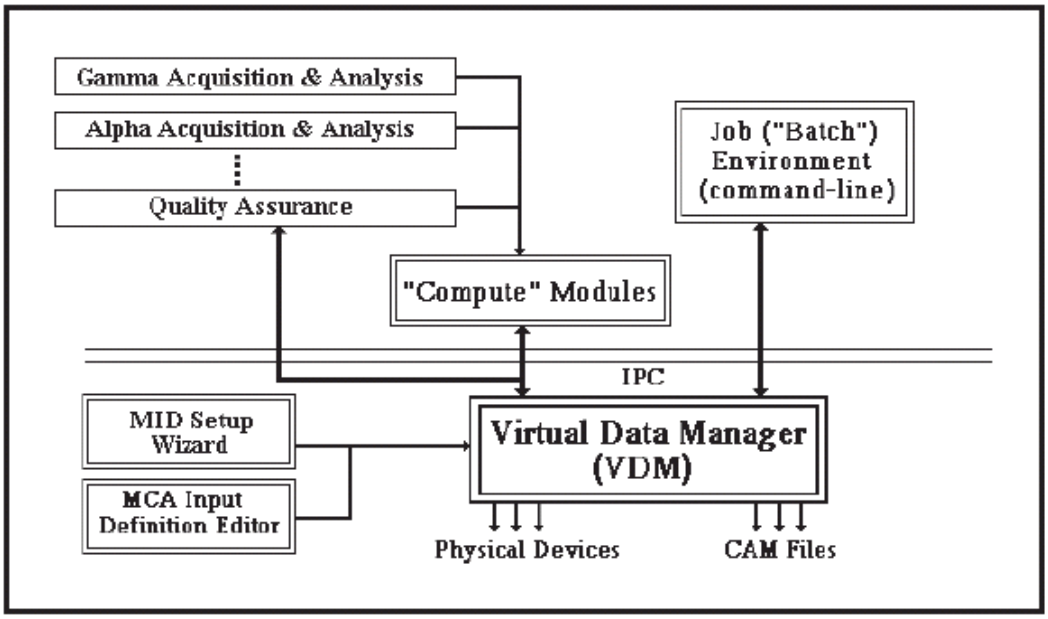

Figure 3.4: The Genie-2000's Architecture [59].

3.2.4 Measurements of Transmitted Gamma-ray Spectra

3.2.4.1 Experimental Configuration

The transmission gamma-ray measurements are composed of two parts dealing with the two gamma-ray sources. The first part was using a 2 mCi Cs-137 source with all samples

listed in Table 3.1, while the second part was using a 1.2 mCi Co-60 source. The same method was applied for both parts.

The experimental arrangement for the gamma-ray measurements is given in Figure 3.5.

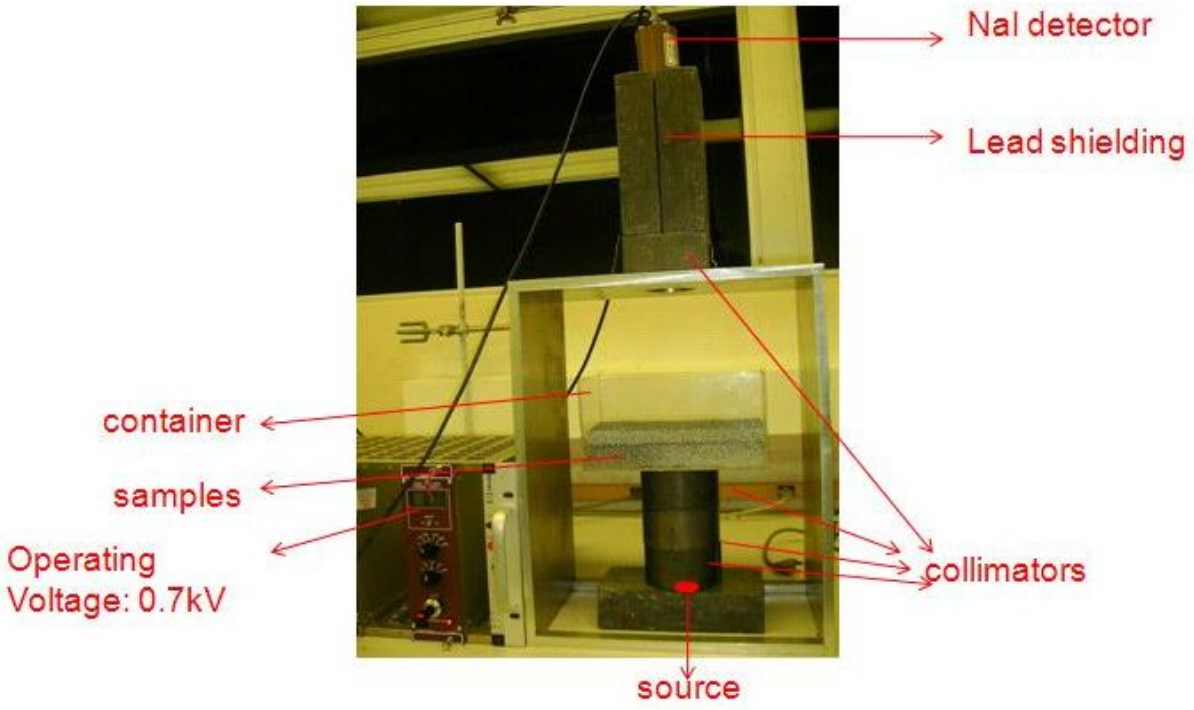

Figure 3.5: Gamma-ray experimental configuration.

Figure 3.5 shows the real experimental configuration. A steel stand was made to provide stability for the whole set-up. The samples held in a plastic container were placed between the source and detector. In each measurement, gamma-rays were emitted from a radioactive source, which was housed in a lead collimator with other two collimators above.

To minimize the effects of background radiation, the detector was provided with adequate lead shielding. During testing, two blocks of concrete were placed in front of the stand for shielding between source and people.

For accuracy of the measurements and attenuation coefficients which would be calculated according to the results of measurements, the distance between the source and the detector was determined as 45 cm. Four lead collimators were used to assure a good narrow beam geometry. More details about the geometry and solid angle calculation are talked about in the following section.

3.2.4.2 Geometry Effect

If the total absorption coefficient is to be measured, it is necessary to establish a "good geometry" in order to achieve conditions for narrow-beam geometry. Conditions considered good and bad are illustrated in Figure 3.6. Gamma-rays from the source have been well collimated so that only a narrow beam strikes the absorber. Compton scattered radiation produced is then preventing from reaching the detector by additional shielding [60].

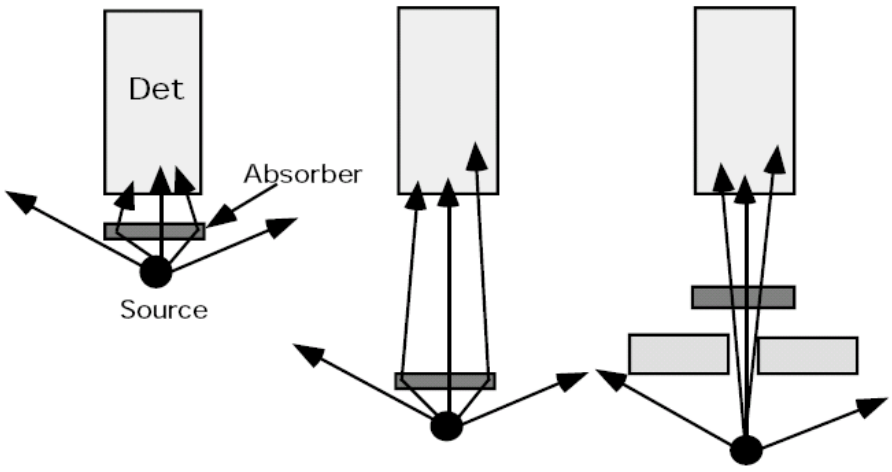

(a) Poor geometry (b) Better geometry (c) Good geometry

Figure 3.6: Illustration of geometry conditions [60].

When the geometry is “poor”, the attenuation is called “broad-beam”. Such conditions are shown in Figure 3.6(a), where Compton scattered radiation from the absorber as well as from the shield strikes the detector. Measured activities will be higher under poor conditions than under good conditions since the attenuation is less. Thus, to establish a good geometry is an important issue considered before setting up this experiment.

The geometry may affect the measurement in two ways. First, the medium between the source and the detector may scatter and may also absorb some particles. Second, the size and shape of the source, collimators and the detector, and the distance between them determine what fraction of particles will enter and have a chance to be counted [1].

Considering a point source at a certain distance from a detector shown in Figure 3.7, since the particles are emitted by the source with equal probability in every direction, only part of them have a chance to enter the detector and be counted. This portion is equal to the fractional solid angle subtended by the detector at the location of the source [1]. The solid angle is defined by:

$$\Omega = \frac{\text{number of particles per second emitted inside the space defined by the contours of the source and the detector aperture}}{\text{number of particles per second emitted by the source}} \qquad (3.1)$$

For a large solid angle, the contribution of multiple scattered photons is considerable even at one mean free path thickness of the medium. When the solid angle is decreased, the multiple scattering is reduced. For a very fine beam, the effect of multiple scattered photons is reduced.

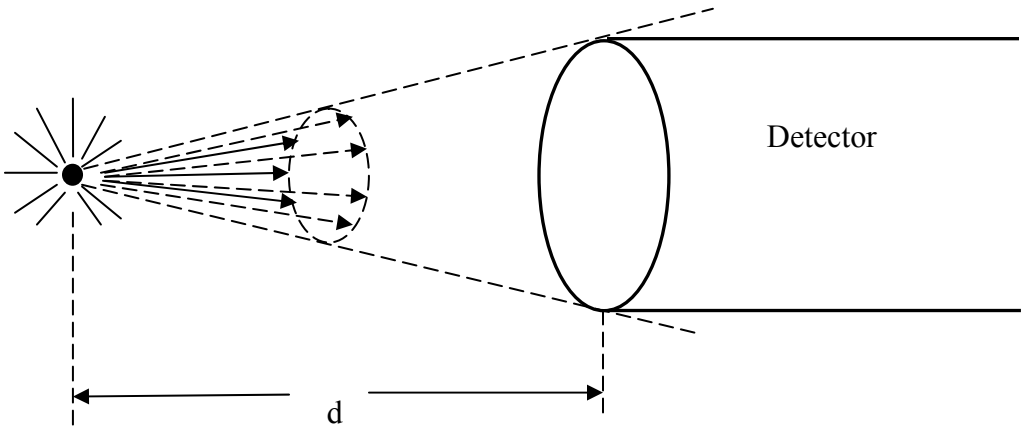

Figure 3.7: The schematic of solid angle definition [1].

According to the conclusions of some research work which has studied the effect of collimator size and absorber thickness on gamma ray attenuation measurements, the effect of multiple scattered photons can be minimized by considering well collimated narrow beam geometry. By reducing the collimator size, i.e. the source to detector solid angle, the effect of multiple scattered photons can be neglected even up to a larger absorber thickness. By optimizing the solid angle for a given absorber thickness, the attenuation coefficient can be measured accurately [61].

"Good geometry" also depends on the sample. Theoretically, the incident beam should be narrow enough to avoid secondary scattering (mainly as the result of one or more Compton scattering) to reach the detector. On another hand, from a practical point of view, the aperture should not be too small, since it will give a relatively low count rate and too long counting time. Materials in which there is an appreciable variation in density over distance of the order of 100nm (voids) give rise to small-angle scattering. The aperture

therefore should be opened a little to encompass the cone of small-angle scattering (Leif Gerward, 2007). In this experiment, collimators with appropriate aperture size were chosen for this consideration.

A simplified schematic of the experimental configuration is shown is Figure 3.8.

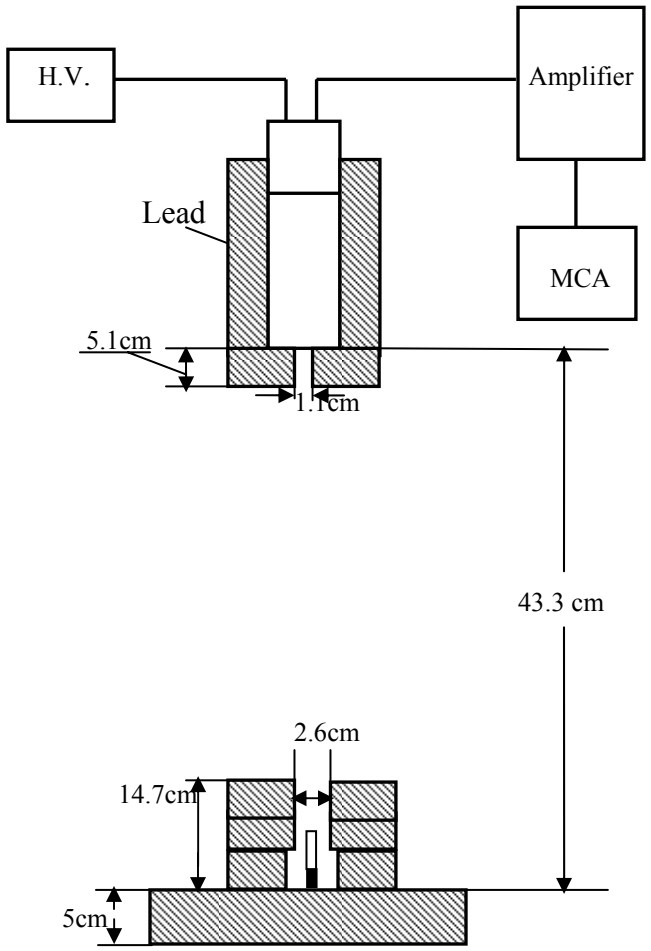

Figure 3.8: Gamma-ray experimental setup of the transmission method.

The source with 0.4 cm diameter was located at the tip of a 5.25 cm long rod. In this experiment, in order to evaluate the geometry of the setup, the source was treated as a disk

source to calculate solid angle. The equation to calculate the solid angle for a disk source parallel to a detector with a circular aperture is [1]:

$$\Omega = \frac{\omega^2}{4}\{1 - \frac{3}{4}(\varphi^2 + \omega^2) + \frac{15}{8}(\frac{\varphi^4 + \omega^4}{3} + \varphi^2\omega^2) - \frac{35}{16}[\frac{\varphi^6 + \omega^6}{4} + \frac{3}{2}\varphi^2\omega^2(\varphi^2 + \omega^2)]\} \quad (3.2)$$

$$\varphi = R_s / d \quad (3.3)$$

$$\omega = R_d / d \quad (3.4)$$

where d is the distance from the detector to the source, R_d is the radius of the detector's aperture and R_s is the radius of the disk source. Here d is measured as 43.3 cm. R_d, which is the diameter of the aperture of the collimator below the detector, is 1.3 cm. R_s is 0.2 cm. By substituting these values into equation 3.2, the solid angle is calculated as 5.633E-05 Sr. Compared with the literature [14] [61], the geometry of this setup could be evaluated as a "good narrow beam geometry".

3.2.4.3 Measuring Approach

After establishing this narrow beam gamma-ray transmission geometry, the attenuation measurements were carried out with the prepared samples in the configuration described above.

The samples, which were put in a plastic container, were stacked on top of each other placed one by one to get various thicknesses. For sample systems with different thickness and material, measurements were performed. The intensities of transmitted photons were measured without (I_0) and with (I) placing the samples in the container. Appropriate counting time (fixed preset time was set as 90s in the Genie 2000 software) for each measurement was chosen after trials so that 10^5-10^6 counts were recorded under each photo peak. Hence the

statistical uncertainty was kept below ~0.3%. The first run was conducted using bulk samples with different thicknesses. The second run of measurements was repeated in the situation of adding water into the container to fill the foam samples. Another run was performed with ^{137}Cs source, by filling 2% (w/v) boric acid solution into the foam samples. The experiments were conducted at constant temperature to avoid any shift of peak. In order to check the performance of the experimental set up, the linear attenuation coefficients of pure aluminum plates were calculated using experimental results and compared with theoretical data.

3.3 Thermal Neutron Transmission Measurements at the NCSU PULSTAR Reactor

3.3.1 General Description of The PULSTAR Reactor

The North Carolina State University PULSTAR Reactor is a light water moderated and cooled research reactor using 4% enriched sintered UO_2 pellet fuel. The reactor is used for a variety of purposes including training and research and operates at a steady state power level of 1MW (thermal) [62].

The PULSTAR Reactor core is comprised of 25 fuel assemblies, ten graphite reflectors and three control rods mounted on a core grid plate approximately 7.3 m (24ft.) below the open pool water surface. Storage is provided for spent / unirradiated reactor fuel at the base of the pool [63].

A fuel assembly is comprised of 25 fuel rods in a 5×5 array with a surrounding Zircalloy channel and aluminum fittings. Each fuel rod is comprised of forty uranium dioxide

pellets enriched to 4%, stacked in a Zircalloy tube. The active fuel length is 61 cm (24in). The fuel assemblies are provided with end fittings to position them on a 6×6 core grid plate. The end fitting, or “nosepiece”, is eccentric with respect to the center of the box. This allows the fuel assembly to be mounted in two different orientations in any of the 36 grid plate positions so the control rods can be located between alternate rows of fuel assemblies [63].

The graphite reflectors are constructed from solid blocks of graphite fitted with aluminum corner braces and a nosepiece to position them on the core grid plate. As with the fuel assemblies, the center line of the reflector nosepiece is eccentric with respect to the center of the box. The active graphite reflector length is 66 cm (26 in) [63].

Reactor control is provided by use of three control rods and one pulsing rod. The rod drive mechanisms are in-line units located on the bridge structure above the pool water surface.

The reactor is equipped with five beam ports that terminate at the boundary of the core and one through port. Beam tubes (BT) BT1, BT2, BT4 and BT5 are 6" diameter, while BT3 is 8" diameter and BT6 is a 12"×12" port. There is a heavy U-235 core load (about 12.5 kg) and a low moderator-fuel ratio. This and the core design leads to peaking of the thermal flux at the core boundary. Figure 3.9 shows the layout of the reactor core region, showing the position of the fuel assemblies, graphite reflectors, and control rods [64]. Figure 3.10 is a schematic of various beam tubes [65]. It shows the BT5 is the radial beam tube with a direct line of sight at the core.

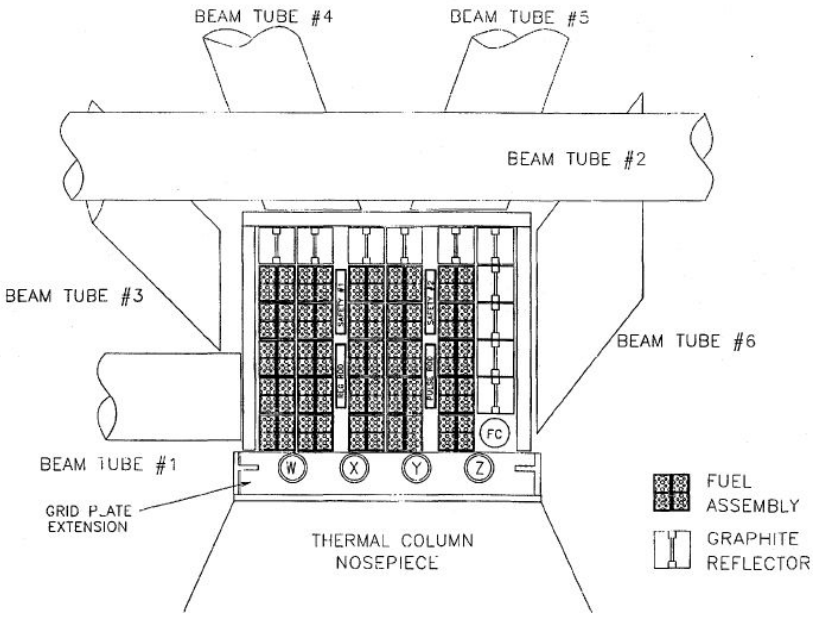

Figure 3.9: Horizontal cross-section of the PULSTAR 5×5 reflected core [63].

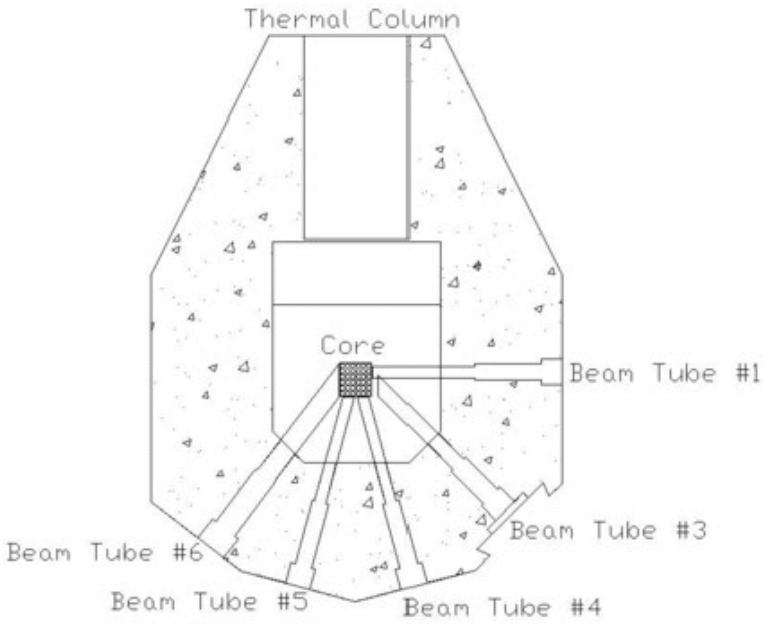

Figure 3.10: Various beam tubes. Beam tube #2 which is a through tube is not shown in this figure [65].

3.3.2 Neutron Detection

3.3.2.1 The ^{3}He(n, p)t Reaction

Neutrons have mass but no electrical charge. Because of this they cannot directly produce ionization in a detector, and therefore cannot be directly detected. This means that neutron detectors must rely upon a conversion process where an incident neutron interacts with a nucleus to produce a secondary charged particle. These charged particles are then directly detected and from them the presence of neutrons is deduced.

Neutrons are generally detected through nuclear reactions that result in prompt energetic charged particles such as protons, alpha particles, and so on. Virtually every type of neutron detector involves the combination of a target material designed to carry out this conversion together with one of the conventional radiation detectors. Different techniques are employed for neutron detection in different energy regions, for the reason that the cross-section for neutron interactions in most materials is a strong function of neutron energy.

In this work, the neutrons of interest for now are in the energy range below the cadmium cutoff of about 0.5 eV [7]. All common reactions used to detect neutrons in this conventionally called slow neutron region result in heavy charged particles. Possible reaction products are listed below [7]:

target nucleus +neutron → { recoil nucleus; proton; alpha particle; fission fragments }

^{3}He counter was used in these measurements for the detection of thermal neutrons.

The ^{3}He(n, p)t reaction is probably the most commonly employed reaction for high efficiency thermal neutron today. The cross-section for ^{3}He is quite high, 5327±10 b for thermal neutrons (at v_0=2200 /sec) and varies as 1/v. The gas ^{3}He is used as a detection medium for neutrons through the reaction:

$$ {}^3_2He + {}^1_0n \rightarrow {}^3_1H + {}^1_1p \qquad \text{Q-value} = 0.764 \text{ MeV} $$

A typical position sensitive ^{3}He proportional tube is filled with ^{3}He gas. Electrons due to ionization in the fill gas by the reaction products are accelerated to the anode by the detector bias. The positive ions are then drifted towards the cathode resulting in an equal but opposite charge being deposited on the anode and cathode [66].

The pulse height spectrum from the interaction of a thermal neutron in a typical ^{3}He neutron detector will look as shown in Figure 3.11 [67].

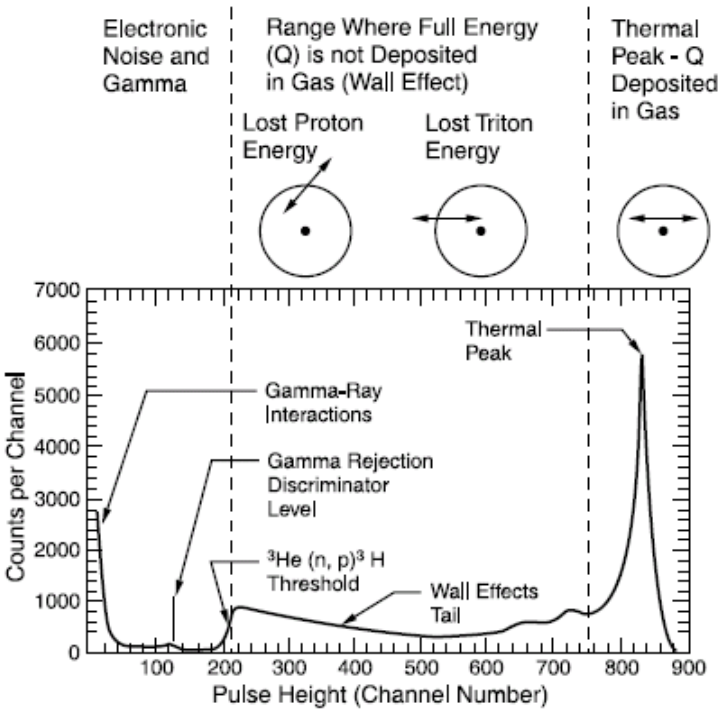

Figure 3.11: Thermal Neutron Induced Pulse Height Spectrum from a moderated ^{3}He detector [67].

3.3.2.2 Counting Electronics

Figure 3.12 shows a schematic of the counting electronics used in the neutron experiment.

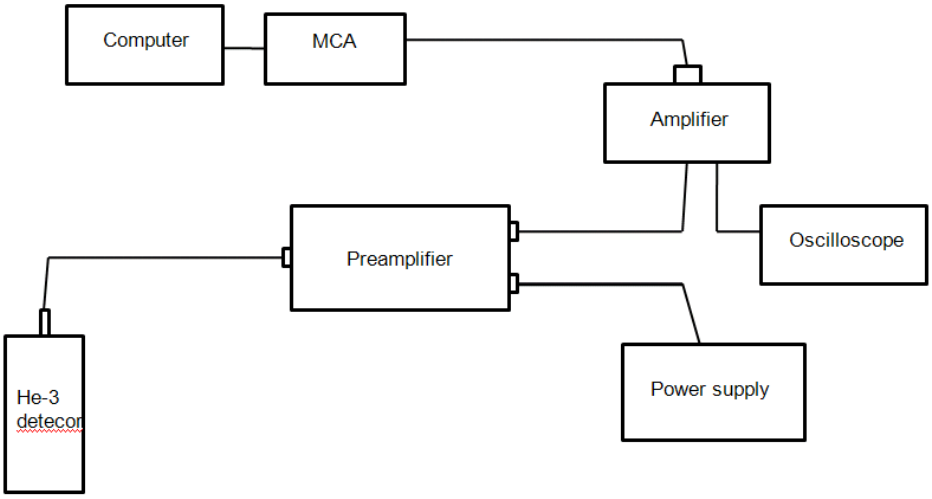

Figure 3.12: Schematic of electronics in thermal neutron transmission experiments.

The electronics used:

- Detector: ^{3}He proportional tube
- Bin: ORTEC Model 401A
- Preamplifier: Ortec Model 142 PC
- Amplifier: Ortec Model 485
- Oscilloscope: Tektronix TDS 2244 4 channel digital real-time oscilloscope
- High Voltage Power Supply: Ortec Model 556

  Operating Voltage: 1 kV
- Multichannel analyzer (MCA): Amptek MCA-8000A Pocket MCA

The circuit shown in Figure 3.12 is used to measure the rate of pulses from the ^{3}He detector. The pulse of a preamplifier (typically a few hundreds of millivolts) is processed through a linear amplifier. Amplifier provides voltage gain to the preamplifier pulses, so that

the rate of pulses can be counted easily. In order to make sure the pulse is good and proceed with the measurements, an oscilloscope was used to check the quality of the signal as well as the level and type of the electronic noise. A multichannel analyzer (MCA) recorded and stored the pulses, which were then analyzed by the computer software.

Figure 3.13 shows the ^{3}He detector with a polyethylene surrounding and MCA used in the measurements.

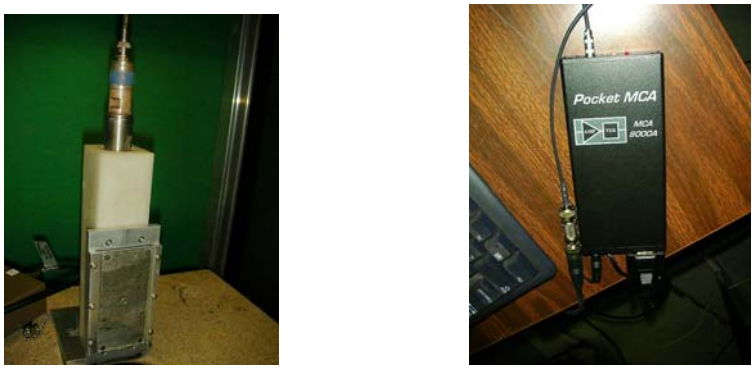

Figure 3.13: ^{3}He detector and the MCA equipment.

3.3.3 Data Acquisition Method

The Pocket MCA Software (PMCA), ADMCA Analog and Digital Acquisition Version 1, 0, 0, 16, was used in these measurements to obtain the transmitted neutron spectroscopy. This AMPTEK ADMCA windows software provides control of the MCA-8000A and supports region of interest (ROI), energy calibration, peak search, peak information, MCA-8000A configuration, multiple spectra, and mathematical operations [68].

The PMCA software acquires and displays all data transmitted by the MCA-8000A: spectral data, elapsed real and live time, and status parameters and flags, including battery status.

3.3.4 Measurements

3.3.4.1 Experimental Configuration

In order to get results as accurate as possible, the experiments must be carried out with “good geometry”. Good geometry is best achieved by locating the detector as far from the source as possible and by making the detector and sample small. In these measurements, the detector-to-source distance is measured as 130.125".

The experimental arrangements and a schematic are given below to illustrate the geometry.

The ^{3}He detector, three cadmium collimators, and a boron collimator were aligned before doing the measurements.

Figure 3.15 shows the close-up of the beam port where the beam is emitted. It keeps rotating during operating and its center locates 36" above the floor.

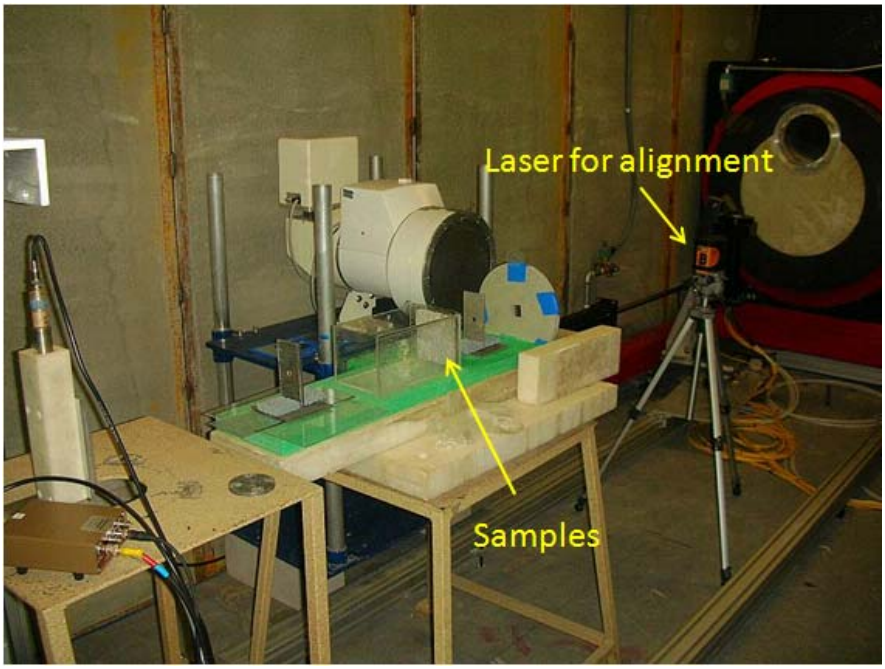

Figure 3.14: Alignment before measurements.

Figure 3.15: Close-up of the thermal neutron beam port.

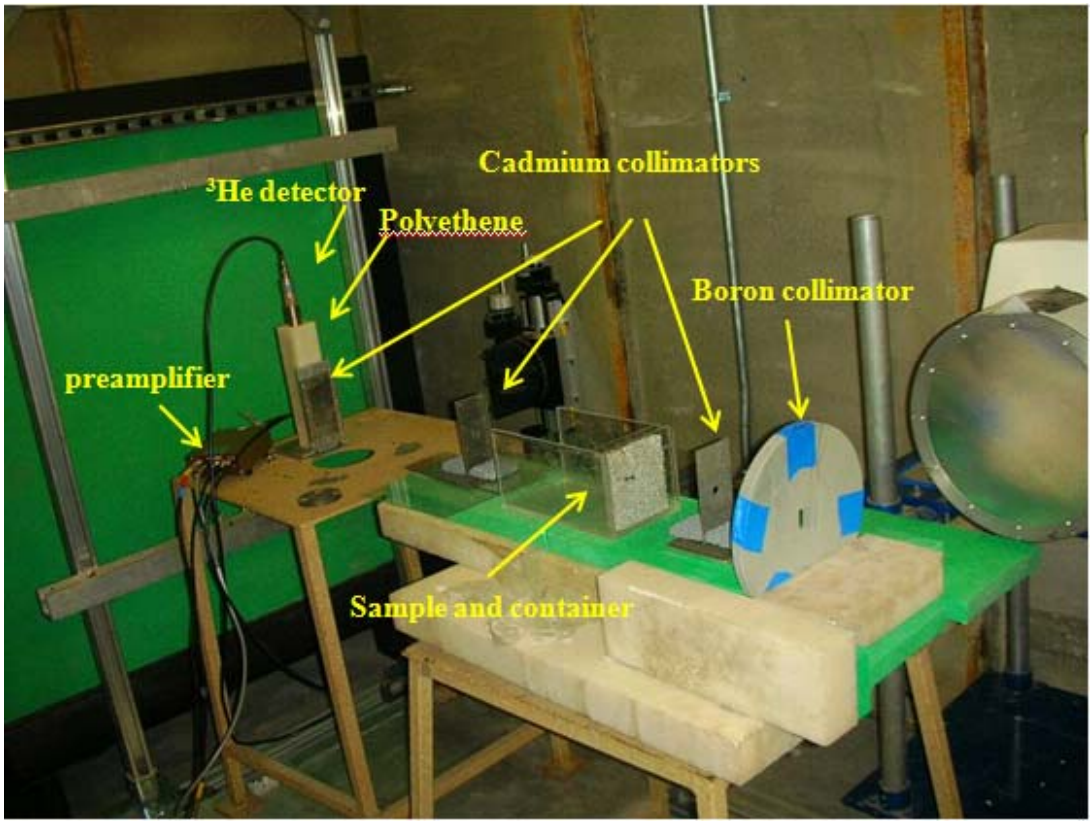

Figure 3.16: Inside view of the experimental configuration.

The amplifier, oscilloscope, MCA and computer were connected by cables and placed outside the shuttle.

As Figure 3.16 shows, all the equipments were put above two tables. The ^{3}He detector was surrounded by a 2"×2" polyethene holder. Totally three cadmium collimators and a boron collimator were placed between the detector and the beam. The centers of the apertures of all the collimators were located at 36" above floor, in order that the collimated narrow beam could go through the apertures to reach the detector during operation of the shuttle.

Figure 3.17 illustrates the measured geometry by a schematic.

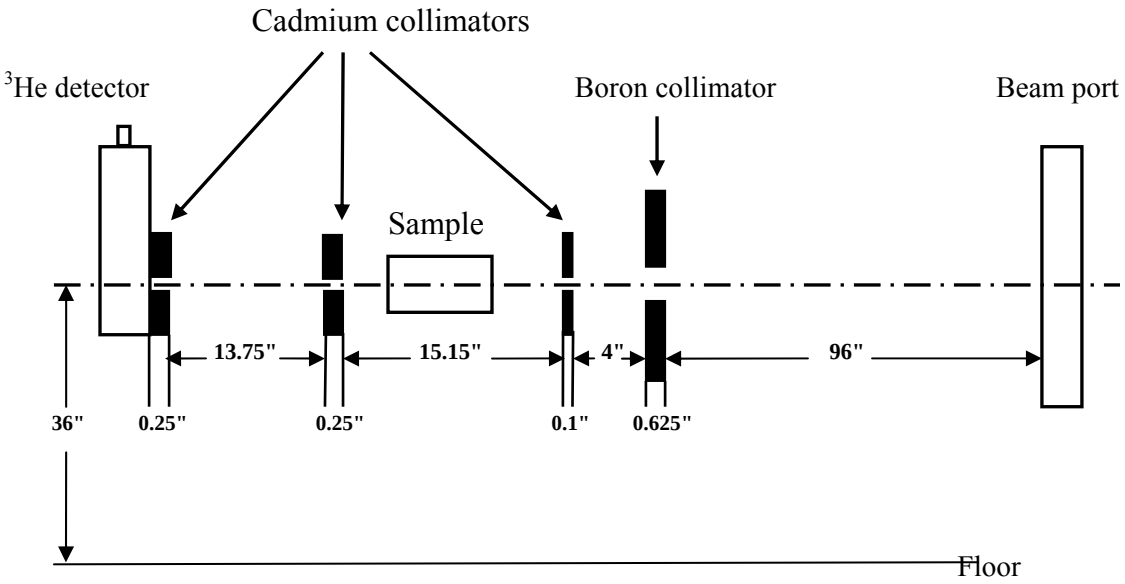

Figure 3.17: Schematic of the experimental geometry.

3.3.4.2 Energy Spectrum

For neutrons produced in a reactor, the flux consists of neutrons that have an energy spectrum extending up to some maximum energy.

In this work, the neutron radiation source used is a polyenergetic thermal neutron beam from the PULSTAR reactor. A thermal neutron is a free neutron with a kinetic energy of about 0.025eV (a speed of 2200 m/s) which is the most probable energy at a temperature of 290 K (17ºC or 62ºF), in a Maxwell-Boltzmann distribution for this temperature. It is conventionally to specify slow neutron cross-sections at this velocity, which corresponds to energy of 0.0253 eV [69].

Thermal neutrons are nearly in thermodynamic equilibrium with the thermal motion of the moderator atoms; their energy distribution can frequently be approximated by a Maxwell distribution with a neutron temperature somewhat higher than the moderator temperature.

The measured total neutron flux at the beam port entry is $\sim 2.5 \times 10^{12}$ n/cm^2·sec at full power (1 MW). The measurement of the neutron flux was performed using cobalt foil activation [65]. Figure 3.18 is the energy spectrum of neutrons at the entry of beam tube, calculated using MCNP by Kaushal Kishor Mishra. The Y-axis in the figure gives the probability density function of the particle flux with respect to energy normalized to a maximum unity. From the neutron spectrum, it can be clearly observed that the neutron beam is sufficiently thermalized [65].

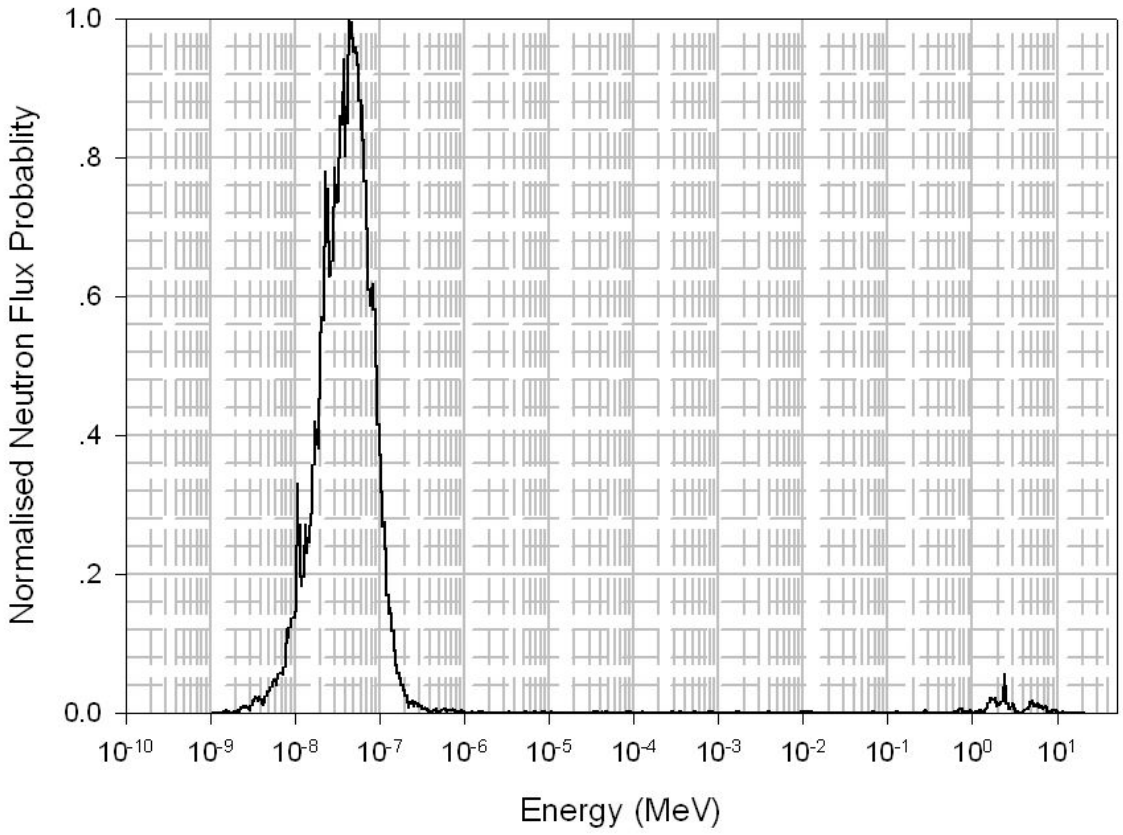

Figure 3.18: The neutron energy spectrum at the entry of BT #5 as calculated using MCNP [65].

3.3.4.3 Measuring Approach

After the narrow beam geometry was established, transmission measurements were carried out for the sample placed in the direct beam.

The software Labview was used as a computer interface with measurement hardware to control the operation of the beam shutter.

The reactor's full power is 1MW, which is so high that it will saturate the detector. After trying different power levels, 5 kW was determined as the operation power level for the measurements.

The samples, which were put in the same plastic container as used in gamma-ray measurements, were placed one by one for different thicknesses between the source and the detector. For sample systems with different thicknesses and materials, measurements were performed. The intensities of transmitted neutrons were measured without (I_0) and with (I) placing the samples in the container. Intensities of neutrons were measured on MCA for fixed preset time (300s) for each counting by selecting a region of pulse height spectrum containing the thermal peak. The second run of measurements was repeated in the situation of adding water into the container to fill the foam samples. Another three runs were performed with by filling 1%, 2%, 3% (w/v) boric acid solution respectively into the foam samples.

The experiments were conducted in the environment with a constant temperature of 70 ºF and a 40% humidity to avoid any shift of peak.

An important consideration is the discrimination against gamma-rays, which often are found together with the neutron flux to be measured. This gamma radiation is produced partly in the fission process and partly in the process of neutron capture in structural materials; a part also comes from the radioactive daughter products of the primary fission fragments [70]. In this experiment the gamma flux leakage from outside the beam defining volume needs to be considered. Gamma-rays interact primarily in the wall of the counter and create secondary electrons that may produce ionization in the gas. Because the stoPPIng power for electrons in gases is quite low, a typical electron will deposit only a small fraction of its initial energy within the gas before reaching the opposite wall of the counter [7]. Thus, we should expect that most gamma-ray interactions will result in low-amplitude pulses that

will lie in the tail to the left of "Gamma Rejection Discriminator Level" in Figure 3.11. Simple amplitude discrimination can then easily eliminate these gamma-rays without sacrificing neutron efficiency.

In these measurements, the Region of Interest (ROI) was set in the ADMCA software to discriminate gamma-rays. From observation, the ROI was decided as from channel 128 to 1023. Figure 3.19 is an example of the spectrum after discrimination of gamma-rays in one of the measurements.

Figure 3.20 is an example of the report generated of ROI details for the above spectrum.

Background was measured in each counting and subtracted from the total counts (Net Area in Figure 3.21) in later calculations. The background in each counting was measured by attaching a thin cadmium sheet to the boron collimator in Figure 3.16, which removed all the neutrons of the beam. Figure 3.21 shows the spectrum of background in ADMCA in one measurement. Similar ROI report was generated to get the "net area" for background.

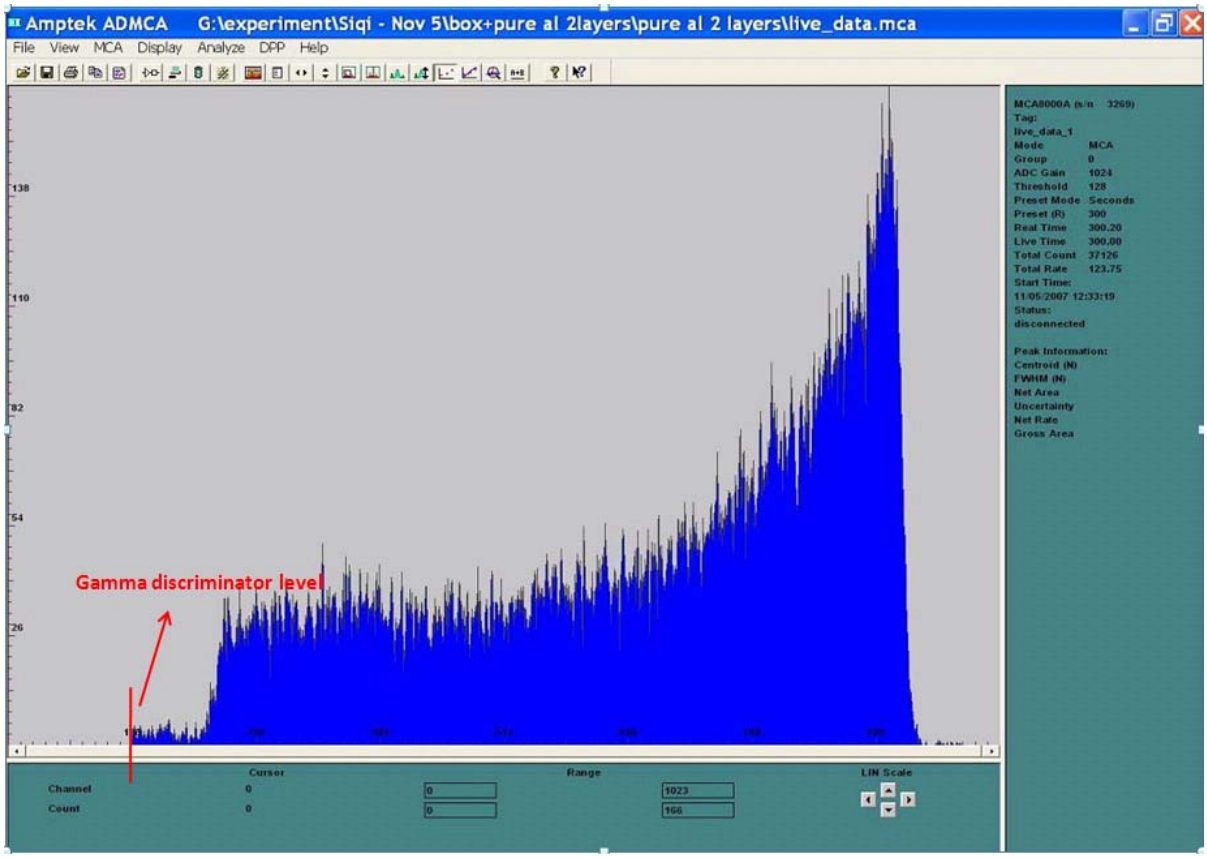

Figure 3.19: An example showing the thermal neutron spectrum after discriminating gamma-rays.

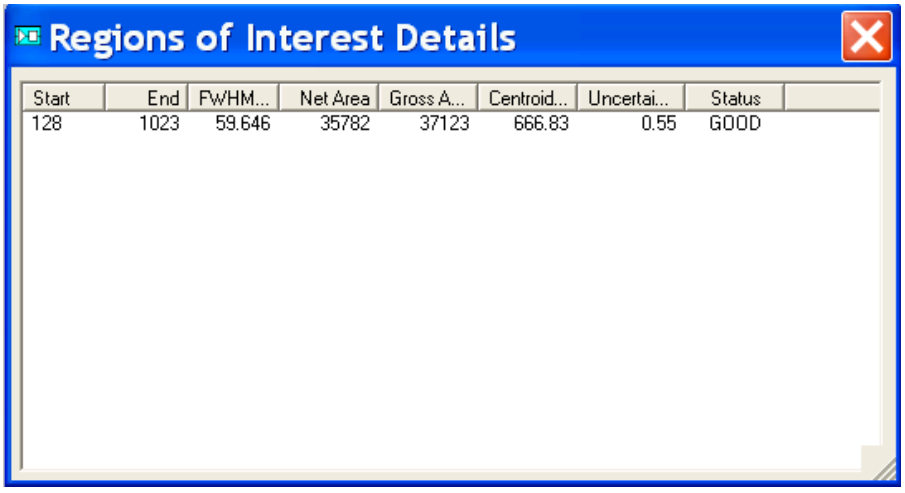

Figure 3.20: An example showing the ROI details.

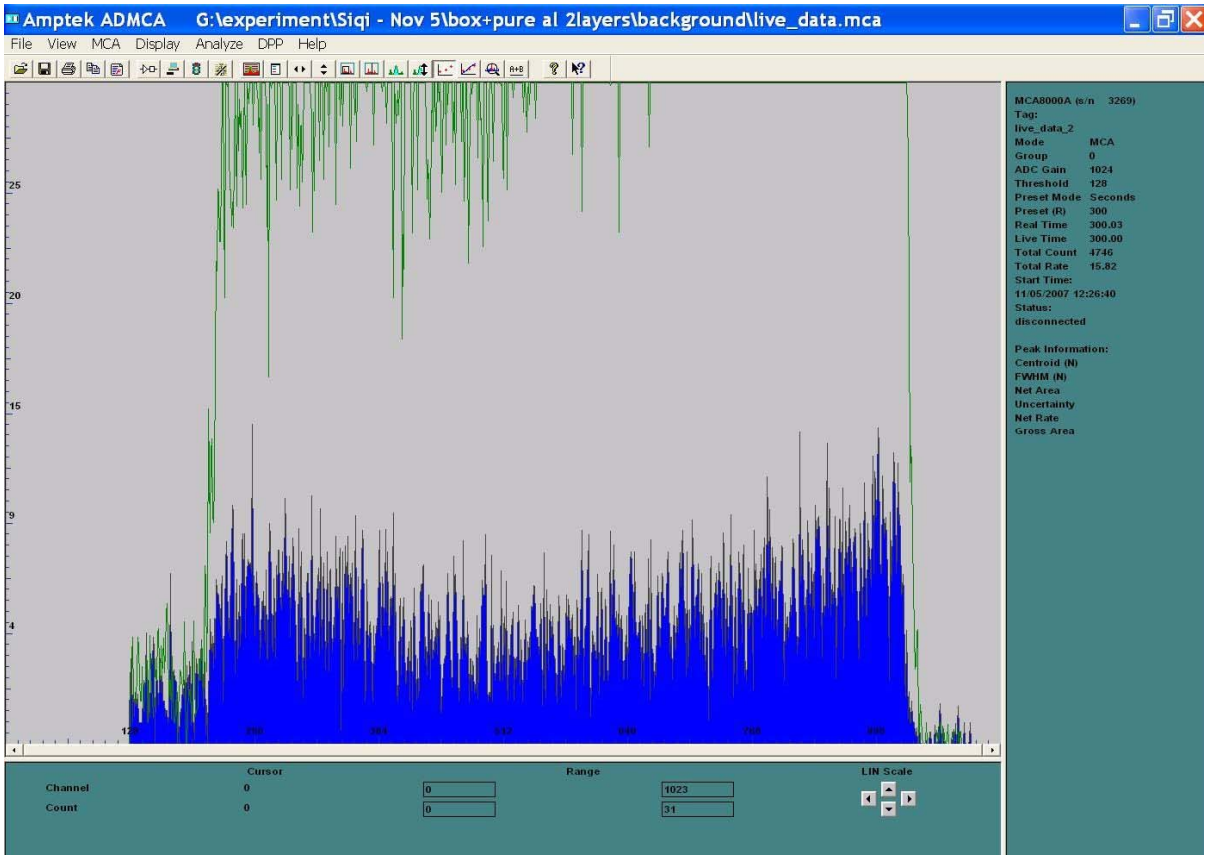

Figure 3.21: An example showing the spectrum of background.

Chapter4 Experimental Results and Discussion

Table 4.1 is a description of the samples used in all the measurements for both gamma-ray and neutron experiments.

Table 4.1: Description of samples.

Shielding sample material	Density (g/cm^3)	Slab thickness selected (inch)
Pure bulk Al	2.7	0.25, 0.5, 0.75, 1, 1.25, 1.5
Bulk Al alloy 6061	2.7	0.25, 0.5, 0.75
10PPI open-cell Al foam	0.216	0.5, 0.75, 1, 1.25, 1.5, 1.75, 2, 2.5
20PPI open-cell Al foam	0.216	0.5, 0.6875, 1, 1.5, 2, 2.6875
10PPI foam + water	1.136	0.5, 0.75, 1, 1.25, 1.5, 1.75, 2.25
20PPI foam +water	1.136	0.5, 0.6875, 1, 1.5, 2, 2.6875
20PPI foam + 2% (w/v) boric acid solution	1.142	0.5, 1, 1.5, 2
10PPI foam + 2% (w/v) boric acid solution	1.142	0.5, 0.75, 1, 1.5, 1.5, 2
10PPI foam + 1% (w/v) boric acid solution	1.139	0.5, 0.75, 1, 1.25, 1.5
10PPI foam + 3% (w/v) boric acid solution	1.144	0.5, 0.75, 1, 1.25, 1.5

The densities of the “foam + liquid” “mixtures” here were estimated by calculation using this equation:

$$\rho = \sum_i v_i \rho_i \tag{4.1}$$

where v_i is the volume fraction of the constituent i in the "mixture".

4.1 Gamma-ray Attenuation Results and Discussion

The intensities of transmitted photons were measured without (I_0) and with (I) placing the samples in the container. The values of net peak area generated in peak reports were recorded as I_0 and I. In Genie 2000, the net peak area for background was reported as zero. Hence the recorded data were directly used in calculation.

4.1.1 Results from Measurements

Tables 4.2 to 4.5 list the recorded data of transmitted intensities and relative uncertainties for each single measurement with the Cs-137 source.

Table 4.2: Transmitted intensities and uncertainty for bulk samples in gamma-ray measurements (Cs-137 source with photon energy 0.662 MeV).

I_0= 1.66E+05				
Sample Materials	Thickness (inch)	Transmitted Intensity (I)	Relative Uncertainty	Transmission ($T=I/I_0$)
Pure bulk Al	0.25	1.47E+05	0.26%	0.886
	0.5	1.30E+05	0.28%	0.783
	0.75	1.16E+05	0.29%	0.699
	1	1.02E+05	0.31%	0.614
	1.25	9.08E+04	0.33%	0.547
	1.5	8.11E+04	0.35%	0.489
Bulk Al alloy	0.25	1.44E+05	0.26%	0.867

Table 4.2 (continued).

6061	0.5	1.28E+05	0.28%	0.771
	0.75	1.12E+05	0.30%	0.675

Table 4.3: Transmitted intensities and uncertainty for foam samples in gamma-ray measurements (Cs-137 source with photon energy 0.662 MeV).

I_0= 1.66E+05				
Sample Materials	Thickness (inch)	Transmitted Intensity (I)	Relative Uncertainty	Transmission ($T=I/I_0$)
10PPI open-cell Al foam	0.5	1.60E+05	0.25%	0.964
	0.75	1.60E+05	0.25%	0964
	1	1.59E+05	0.25%	0.958
	1.25	1.58E+05	0.25%	0.952
	1.5	1.56E+05	0.25%	0.940
	1.75	1.53E+05	0.26%	0.922
	2	1.53E+05	0.26%	0.922
	2.5	1.52E+05	0.26%	0.916
20PPI open-cell Al foam	0. 5	1.61E+05	0.25%	0.970
	0.6875	1.60E+05	0.25%	0.964
	1	1.59E+05	0.25%	0.958
	1.5	1.55E+05	0.25%	0.934
	2	1.53E+05	0.26%	0.922
	2.6875	1.48E+05	0.26%	0.892

Table 4.4: Transmitted intensities and uncertainty for foam samples filled with water in gamma-ray measurements (Cs-137 source with photon energy 0.662 MeV).

I_0= 1.66E+05				
Sample Materials	Thickness (inch)	Transmitted Intensity (I)	Relative Uncertainty	Transmission ($T=I/I_0$)
10PPI open-cell Al foam filled with water	0.5	1.45E+05	0.26%	0.873
	0.75	1.36E+05	0.27%	0.819
	1	1.36E+05	0.27%	0.819
	1.25	1.27E+05	0.28%	0.765
	1.5	1.19E+05	0.29%	0.717
	1.75	1.16E+05	0.29%	0.699
	2	1.08E+05	0.30%	0.651
	2.5	9.88E+04	0.32%	0.595
20PPI open-cell Al foam filled with water	0. 5	1.44E+05	0.26%	0.867
	0.6875	1.37E+05	0.27%	0.825
	1	1.30E+05	0.28%	0.783
	1.5	1.19E+05	0.29%	0.717
	2	1.05E+05	0.31%	0.633
	2.6875	9.03E+04	0.33%	0.544

Table 4.5: Transmitted intensities and uncertainty for foam samples filled with 2% (w/v) boric acid solution in gamma-ray measurements (Cs-137 source with photon energy 0.662 MeV).

I_0= 1.66E+05				
Sample Materials	Thickness (inch)	Transmitted Intensity (I)	Relative Uncertainty	Transmission ($T=I/I_0$)
10PPI open-cell Al foam filled with 2% (w/v) boric acid solution	0.5	1.44E+05	0.26%	0.867
	1	1.30E+05	0.28%	0.783
	1.5	1.14E+05	0.30%	0.689
	2	1.04E+05	0.31%	0.627
20PPI open-cell Al foam filled with 2% (w/v) boric acid solution	0. 5	1.36E+05	0.27%	0.818
	1	1.21E+05	0.29%	0.728
	1.5	1.10E+05	0.30%	0.664
	2	1.00E+05	0.32%	0.603

Tables 4.6 to 4.11 list the recorded data of transmitted intensities and relative uncertainties for each single measurement with Co-60 source.

Table 4.6: Transmitted intensities and uncertainty for bulk samples in gamma-ray measurements (Co-60source with photon energy 1.173 MeV).

I_0= 1.21E+05				
Sample Materials	Thickness (inch)	Transmitted Intensity (I)	Relative Uncertainty	Transmission ($T=I/I_0$)
Pure bulk Al	0.25	1.10E+05	0.30%	0.909
	0.5	1.00E+05	0.32%	0.826
	0.75	9.12E+04	0.33%	0.754
	1	8.46E+04	0.34%	0.699
	1.25	7.62E+04	0.36%	0.630
	1.5	7.02E+04	0.38%	0.580
Bulk Al alloy 6061	0.25	1.09E+05	0.30%	0.901
	0.5	9.91E+04	0.32%	0.819
	0.75	8.95E+04	0.33%	0.740

Table 4.7: Transmitted intensities and uncertainty for foam samples in gamma-ray measurements (Co-60 source with photon energy 1.173 MeV).

I_0= 1.21E+05				
Sample Materials	Thickness (inch)	Transmitted Intensity (I)	Relative Uncertainty	Transmission ($T=I/I_0$)
10PPI open-cell Al foam	0.5	1.19E+05	0.29%	0.983
	0.75	1.17E+05	0.29%	0.967
	1	1.17E+05	0.29%	0.967
	1.25	1.16E+05	0.29%	0.959
	1.5	1.16E+05	0.29%	0.959
	1.75	1.16E+05	0.29%	0.959
	2	1.14E+05	0.30%	0.942
	2.5	1.12E+05	0.30%	0.926
20PPI open-cell Al foam	0. 5	1.18E+05	0.29%	0.975
	0.6875	1.18E+05	0.29%	0.975
	1	1.16E+05	0.29%	0.959
	1.5	1.15E+05	0.29%	0.950
	2	1.13E+05	0.30%	0.934
	2.6875	1.11E+05	0.30%	0.917

Table 4.8: Transmitted intensities and uncertainty for foam samples filled with water in gamma-ray measurements (Co-60 source with photon energy 1.173 MeV).

I_0= 1.21E+05				
Sample Materials	Thickness (inch)	Transmitted Intensity (I)	Relative Uncertainty	Transmission ($T=I/I_0$)
10PPI open-cell Al foam filled with water	0.5	1.09E+05	0.30%	0.901
	0.75	1.07E+05	0.31%	0.884
	1	1.00E+05	0.32%	0.826
	1.25	9.73E+04	0.32%	0.804
	1.5	9.64E+04	0.32%	0.797
	1.75	8.91E+04	0.34%	0.736
	2	8.55E+04	0.34%	0.707
	2.5	7.69E+04	0.35%	0.658
20PPI open-cell Al foam filled with water	0. 5	1.09E+05	0.30%	0.901
	0.6875	1.04E+05	0.31%	0.860
	1	1.02E+05	0.31%	0.843
	1.5	9.26E+04	0.33%	0.765
	2	8.41E+04	0.34%	0.695
	2.6875	7.83E+04	0.37%	0.610

Table 4.9: Transmitted intensities and uncertainty for bulk samples in gamma-ray measurements (Co-60with photon energy 1.332 MeV).

I_0= 1.27E+05				
Sample Materials	Thickness (inch)	Transmitted Intensity (I)	Uncertainty	Transmission ($T=I/I_0$)
Pure bulk Al	0.25	1.17E+05	0.29%	0.921
	0.5	1.07E+05	0.31%	0.843
	0.75	9.85E+04	0.32%	0.776
	1	9.07E+04	0.33%	0.714
	1.25	8.30E+04	0.35%	0.654
	1.5	7.68E+04	0.36%	0.605
Bulk Al alloy 6061	0.25	1.17E+05	0.29%	0.921
	0.5	1.05E+05	0.31%	0.827
	0.75	9.70E+04	0.32%	0.764

Table 4.10: Transmitted intensities and uncertainty for foam sample materials in gamma-ray measurements (Co-60 source with photon energy 1.332 MeV).

I_0= 1.27E+05				
Sample Materials	Thickness (inch)	Transmitted Intensity (I)	Relative Uncertainty	Transmission ($T=I/I_0$)
10PPI open-cell Al foam	0.5	1.24E+05	0.28%	0.976
	0.75	1.25E+05	0.28%	0.984
	1	1.23E+05	0.29%	0.969
	1.25	1.23E+05	0.29%	0.969
	1.5	1.22E+05	0.29%	0.961
	1.75	1.22E+05	0.29%	0.961
	2	1.21E+05	0.29%	0.953
	2.5	1.19E+05	0.29%	0.937
20PPI open-cell Al foam	0. 5	1.25E+05	0.28%	0.984
	0.6875	1.24E+05	0.28%	0.976
	1	1.23E+05	0.29%	0.969
	1.5	1.22E+05	0.29%	0.961
	2	1.20E+05	0.29%	0.945
	2.6875	1.18E+05	0.29%	0.929

Table 4.11: Transmitted intensities and uncertainty for foam sample materials filled with water in gamma-ray measurements (Co-60 source with photon energy 1.332 MeV).

I_0= 1.27E+05				
Sample Materials	Thickness (inch)	Transmitted Intensity (I)	Relative Uncertainty	Transmission ($T=I/I_0$)
10PPI open-cell Al foam filled with water	0.5	1.16E+05	0.29%	0.913
	0.75	1.14E+05	0.30%	0.898
	1	1.07E+05	0.31%	0.843
	1.25	1.05E+05	0.31%	0.827
	1.5	1.03E+05	0.31%	0.811
	1.75	9.71E+04	0.32%	0.765
	2	9.31E+04	0.33%	0.733
	2.5	8.69E+04	0.34%	0.684
20PPI open-cell Al foam filled with water	0. 5	1.16E+05	0.29%	0.913
	0.6875	1.12E+05	0.30%	0.882
	1	1.08E+05	0.30%	0.850
	1.5	9.89E+04	0.32%	0.779
	2	9.16E+04	0.33%	0.721
	2.6875	8.03E+04	0.35%	0.632

4.1.2 XCOM Calculations, Analyses and Discussion

The pure bulk aluminum and bulk 6061 aluminum alloy samples were used as reference materials for comparison. In order to check the performance of the experimental set up, the linear attenuation coefficients of aluminum were obtained from the measured incident (I_0) and transmitted (I) gamma-ray intensities using Equation (2.5), and compared with theoretical data from *American National Standard for Gamma-ray.* It has been found out that the values got from experimental results are in good agreement with the theoretical values. The data is shown in Table 4.12.

Table 4.12 Linear attenuation coefficients in aluminum

Sample	Linear attenuation coefficient (μ) in cm^{-1}					
Pure bulk Al	0.662 MeV		1.173 MeV		1.332 MeV	
	Expt.	Theo.	Expt.	Theo.	Expt.	Theo.
	0.1903±0.0019	0.2018	0.1463±0.0038	0.1534	0.1327±0.0020	0.1437
Bulk 6061 Al	0.1920±0.0075	0.2014	0.1599±0.0039	0.1532	0.1401±0.0103	0.1436

The difference between the experimental and theoretical data may result from systematic errors that may occur because of deviations from a good narrow beam geometry.

The exponential law has been confirmed to hold for pure bulk aluminum slabs at 0.662 MeV, 1.173 MeV and 1.332 MeV, as shown in Figure 4.1, which again verifies the narrow beam geometry at the same time. This figure also illustrates the transmission increases (attenuation decreases) as the photon energy increases, which is in agreement with theory.

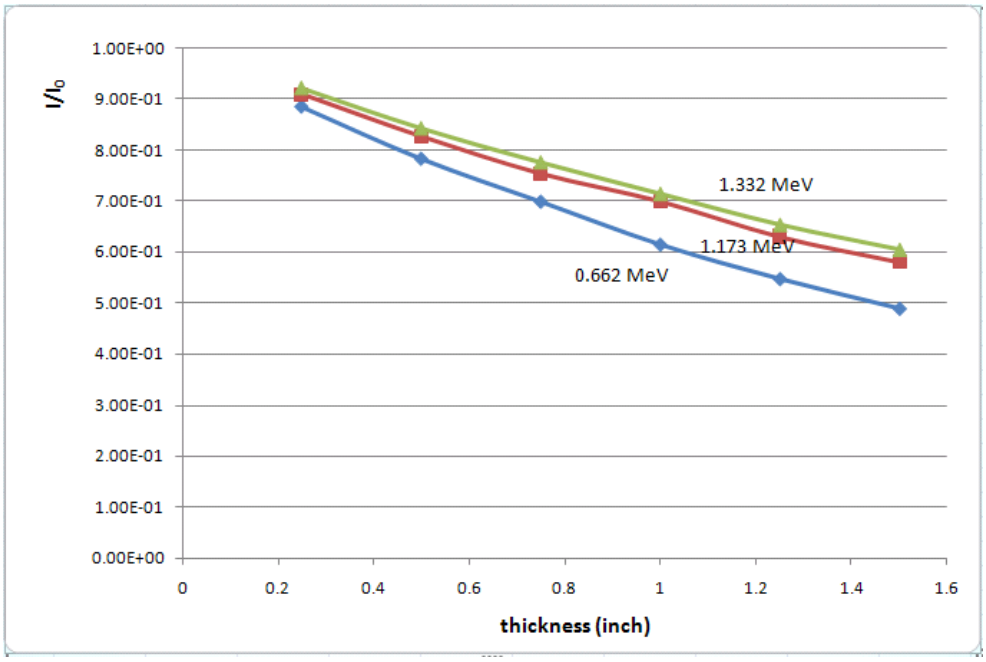

Figure 4.1: The transmission ($T= I/I_0$) vs. thickness for pure bulk Al sample slabs at three different photon energies.

The linear attenuation coefficient and mass attenuation coefficient are basic quantities for determining the penetration of gamma-ray photons in matter. Tabulations of mass attenuation coefficients and interaction cross-sections have been published e.g., by Hubbell and Seltzer (1995), for the elements and a number of substances. A convenient alternative to manual calculations, using tabulated data, is to generate attenuation data as needed via a computer. For this purpose, Berger and Hubbell (1987, 1999) developed a computer program, XCOM.

The web version of XCOM, which can be accessed from the National Institute of Standards and Technology (NIST) Physics Laboratory website, carries out the task to quickly generate the cross sections and attenuation coefficients for elements, compounds and

mixtures, at energy between 1 keV and 100 GeV. The interaction coefficients and total attenuation coefficients for compounds or mixtures are obtained as sums of the corresponding quantities for the atomic constituents. The weighting factors are calculated by XCOM from the chemical formula entered by the user. For mixtures, XCOM requires as input the weight fractions of the constituent elements [71].

Figure 4.1 illustrates the exponential attenuation for three different gamma-ray energies and shows that the transmission increases with increasing gamma-ray energy and decreases with increasing absorber thickness. It should be noted here, at the present energies (0.662 MeV, 1.173 MeV and 1.332 MeV), the attenuation of the incident beam is determined mainly by Compton scattering for the low/middle-Z material aluminum, as shown in Figure 2.2 in the theory section.

Through calculation from tabulated XCOM data, it also shows that Compton scattering contribute more than 99% of the total interaction cross-section at the present three energies. Figure 4.2 is a plot given by XCOM, which can graphically show the Compton scattering domination. As the plot shows, within the shown energy range, this domination begins to decrease faster as the energy increases, approaching 10 MeV. At higher energies (about 16 MeV), pair production starts to dominate up to 100 MeV. Photoelectric absorption contributes the least to the total mass attenuation and decreases with the increasing photon energy.

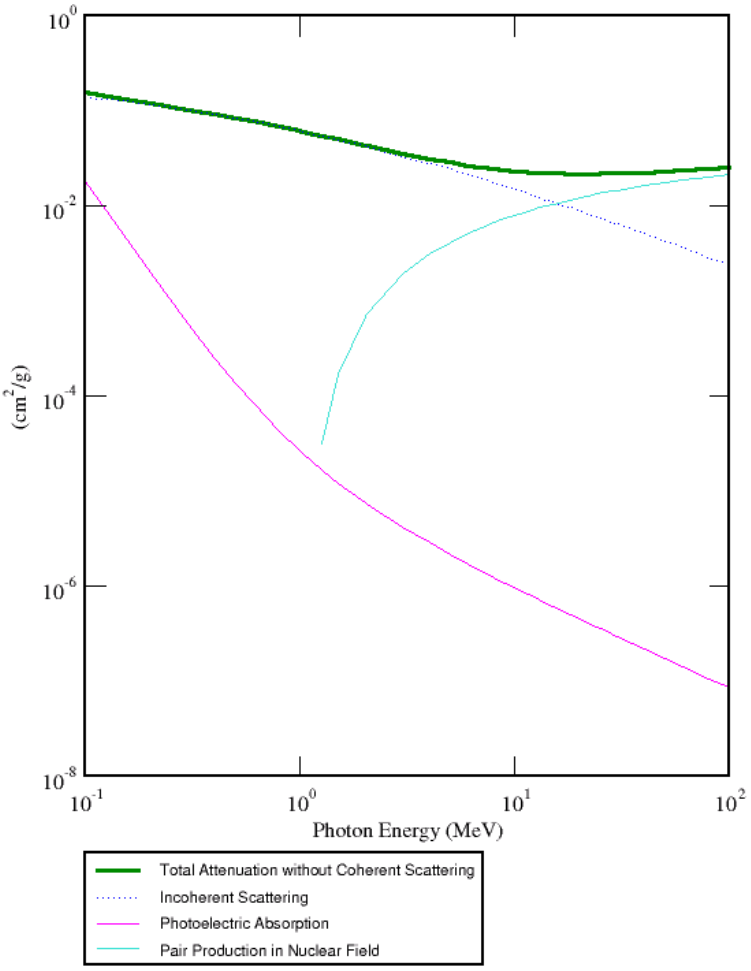

Figure 4.2: Mass attenuation coefficients for aluminum from XCOM results.

The plots of transmission (T) vs. thickness for different sample materials at different energies are shown in the following figures.

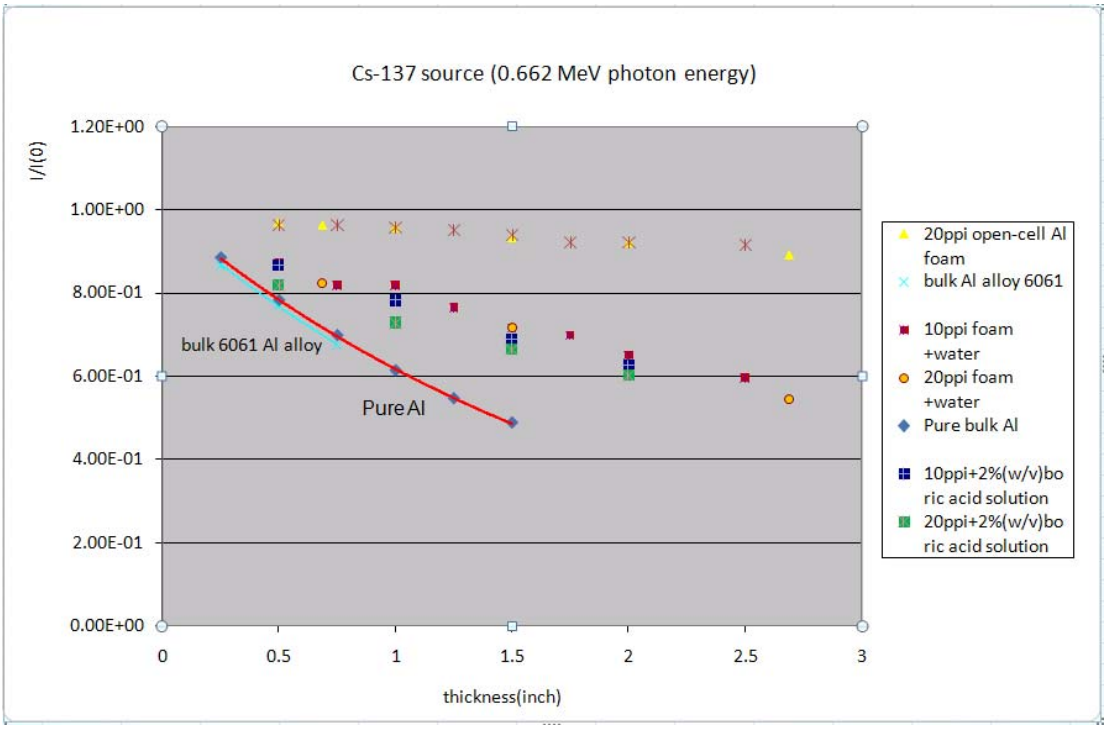

Figure 4.3: Attenuation of samples at 0.662 MeV photon energy.

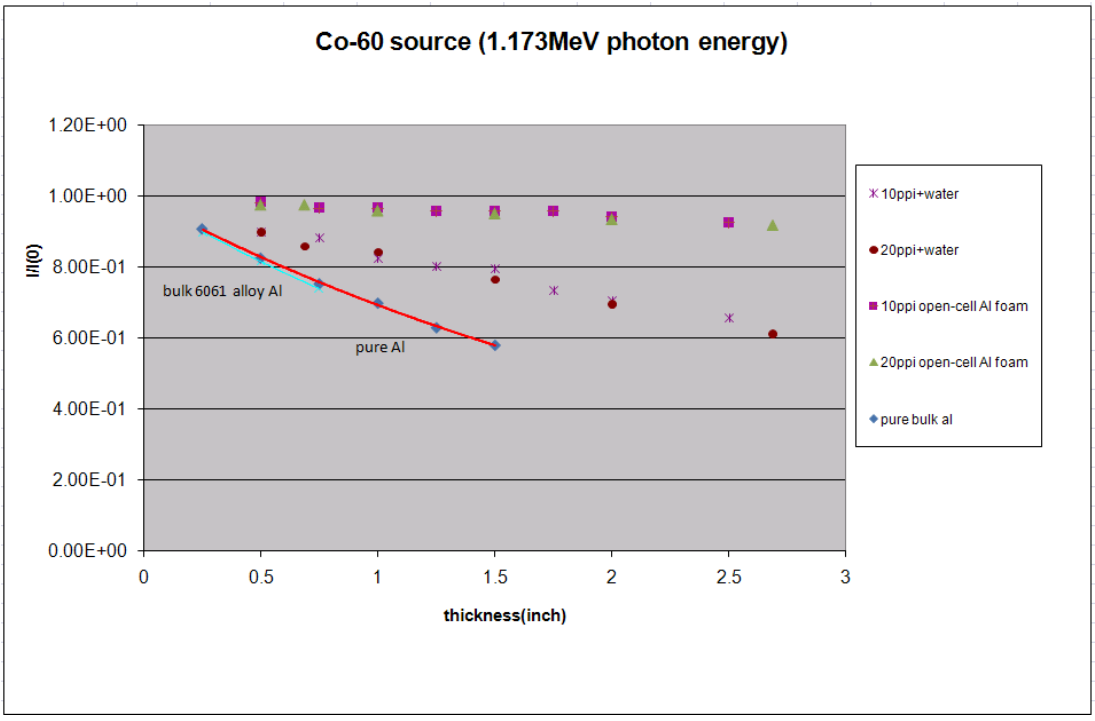

Figure 4.4: Attenuation of samples at 1.173 MeV photon energy.

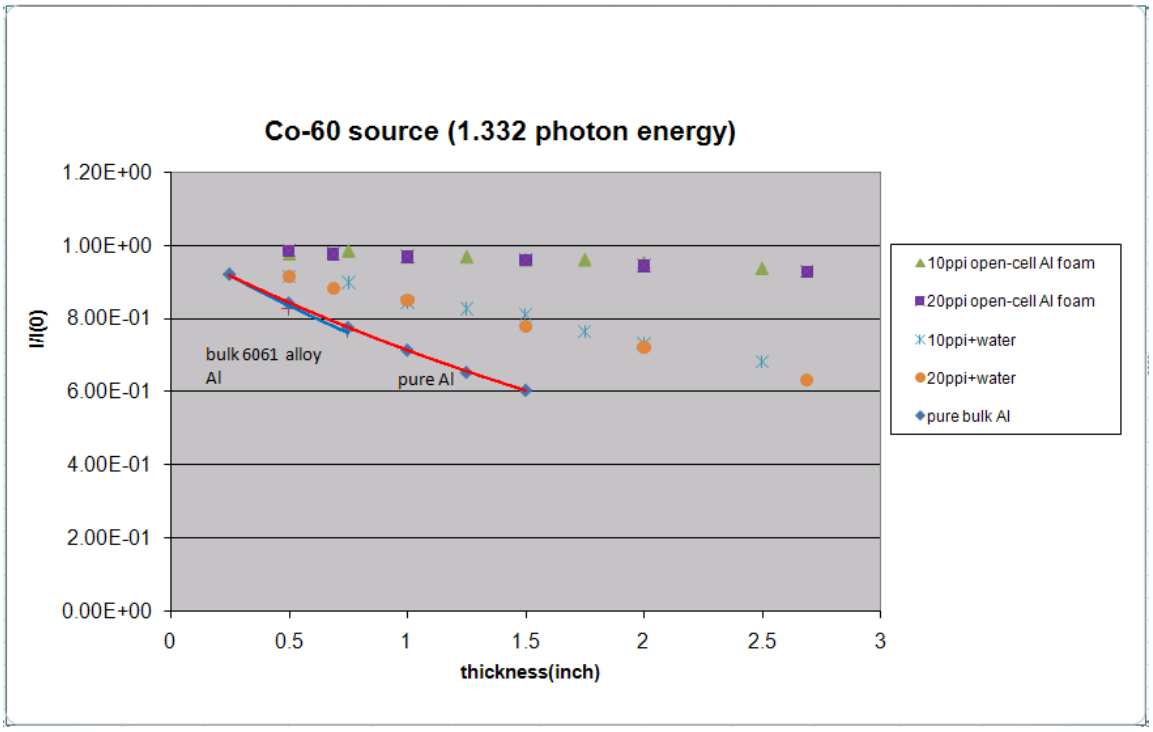

Figure 4.5: Attenuation of samples at 1.332 MeV photon energy.

From Figure 4.3 to Figure 4.5, following conclusions could be drawn:

- For a type of sample material, the transmission increases with the increasing gamma-ray energy, and decreases as the thickness of the sample increases, which means the attenuation increases as the thickness increases.
- For a certain energy, the comparison of attenuation for samples at a certain thickness could be shown as:

  Bulk material > foam filled with liquid > foam
- For bulk material at the three photon energies, the two transmission lines of pure bulk aluminum and bulk 6061 aluminum are quite close to each other, which means the

attenuation for 0.662 MeV, 1.173 MeV and 1.332 MeV gamma-rays are close. But bulk 6061 has a bit better attenuation than pure bulk aluminum.

- For 6101 aluminum foam materials, the figures show that they have the lowest gamma-ray attenuation among all the samples. It can be explained as the foam samples have the lowest density, which is the result from their porous structure. The 10 PPI and 20 PPI foam have close attenuation at all the three energies. The pore size of foam has not shown obvious effect upon attenuation for gamma-rays.
- For "foam + water" sample, the attenuation has shown to be much better than the foam. However, the effect from pore size of foam is not obviously seen either.

This improvement in attenuation might be contributed to the water filled into the foam. These tendencies are consistent with the theory. In the energy range in this experiment, the dominating interaction mechanism is Compton scattering. Therefore the total attenuation is dependent on the total number of electrons as scattering targets in the sample material. Because Compton scattering involves the least tightly bound electrons, the nucleus has only a minor influence and the probability for interaction is nearly independent of atomic number [58]. The interaction probability depends on the electron density, which is proportional to Z/A and nearly constant for all materials [58]. Compared with only foams, the water content in the "foam + water" samples contributes to total electron density of the sample thus increases the total narrow-beam attenuation coefficient.

For "foam + boric acid solution" sample, the measurements were only performed at the lower energy (0.662 MeV). It shows a bit better attenuation than "foam+water" samples.

Now the interest comes to the bulk materials and the “foam + liquid” samples because of the gamma-ray attenuation they’ve shown.

The base material of the Duocel open-cell aluminum foams used in this experiment is bulk 6101 aluminum alloy. Due to the unavailability of the 6101 aluminum alloy samples, no measurements were performed for them. However, with the help of the XCOM program, total attenuation coefficients were calculated with energies from 0.1 MeV up to 100 MeV.

In order to generate the mass attenuation coefficients for the “foam+ liquid” samples, it was assumed that the “foam + water” samples and “foam + 2% (w/v) boric acid solution” samples were “equivalent homogeneous mixtures”. Thus the weight fraction for the constituents were calculated and input in the XCOM program.

First, plot given by XCOM for the equivalent “foam + liquid” mixture shows similar dominating interaction mechanism as that for bulk aluminum, as shown in Figure 4.6 and Figure 4.7.

Through calculation from tabulated XCOM data, it also shows that for both foam with water mixture and foam with boric acid solution mixture, Compton scattering contribute more than 99% of the total interaction cross-section at the present three energies. The data of these two graphs are quite close and similar tendencies are predicted by the plot. Different from bulk aluminum, with the energy range, the Compton scattering dominates at all energies up to domination begins to decrease faster at energies above 10 MeV. At much higher energies (about 80 MeV), pair production starts to dominate up to 100 MeV. Photoelectric absorption contributes the least to the total mass attenuation and decreases with the increasing photon energy.

These tendencies are consistent with the theory. As mentioned in the theory section and Figure 2.2, 2.7 illustrate, Compton scattering dominates up to 100 MeV for the low-Z material. Especially for hydrogen, it interacts with gamma-rays with energy greater than 10 keV almost exclusively by Compton scattering. The reason that compared with bulk aluminum, Compton scattering dominate to higher energies for the "aluminum foam + liquid" samples may be attributed to their hydrogen content.

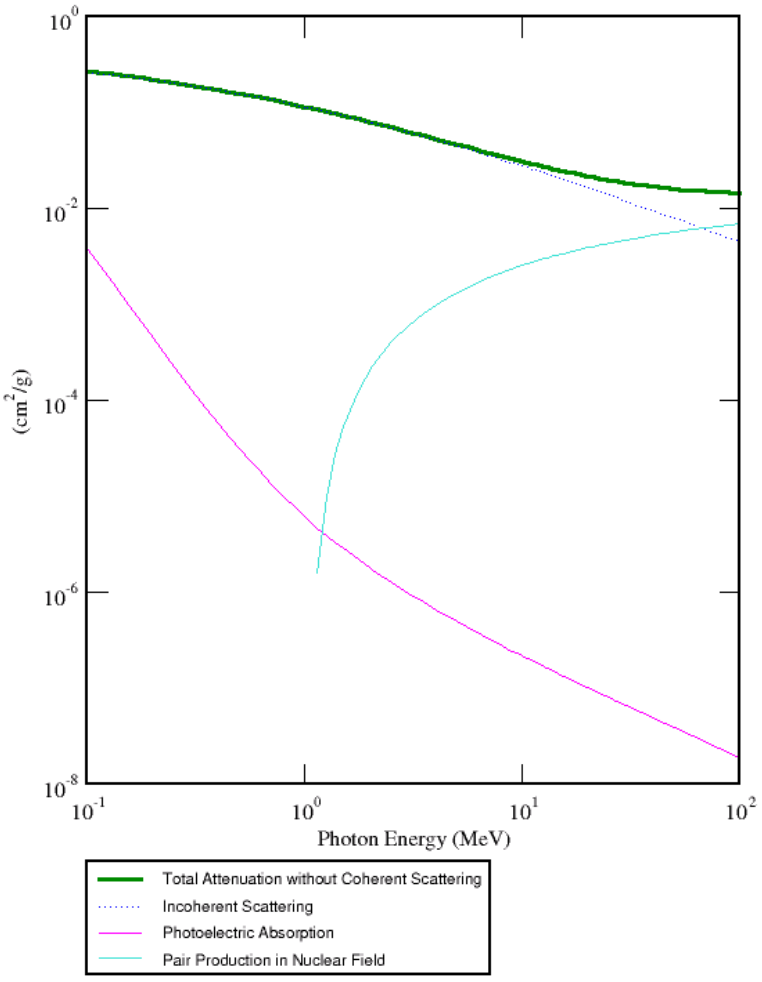

Figure 4.6: Mass attenuation coefficients for foam with water mixture from XCOM results.

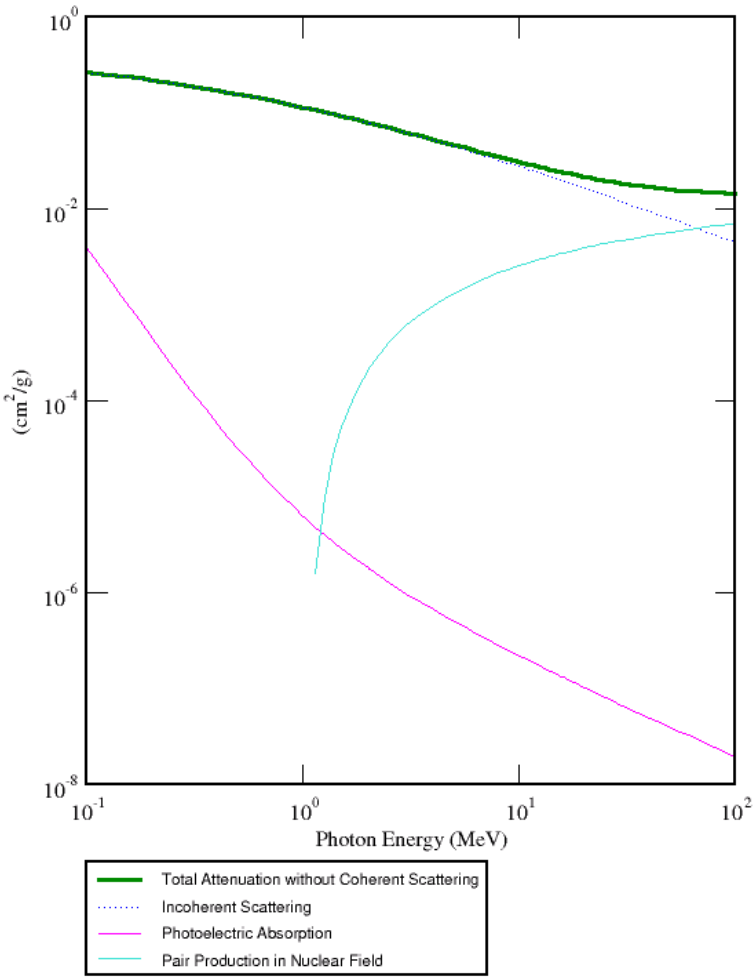

Figure 4.7: Mass attenuation coefficients for foam with 2% (w/v) boric acid solution mixture from XCOM results.

Important parameters such as mass attenuation coefficient could illustrate the ability of gamma-ray attenuation. The quantitative analyses are performed below.

The linear attenuation coefficients and mass attenuation coefficients were calculated from experimental results using Equation (2.5), (2.8) are listed in Table 4.13. The comparison is shown in Table 4.14.

Table 4.13: Linear attenuation coefficients and mass attenuation coefficients from measurements.

Sample	0.662 MeV		1.173 MeV		1.332 MeV	
	μ (cm^{-1})	μ/ρ (cm^2g^{-1})	μ (cm^{-1})	μ/ρ (cm^2g^{-1})	μ (cm^{-1})	μ/ρ (cm^2g^{-1})
Pure bulk Al	0.1903 ±0.0019	0.0705 ±0.0007	0.1463 ±0.0038	0.0542 ±0.0001	0.1327 ±0.0020	0.0491 ±0.0007
Bulk Al alloy 6061	0.1920 ±0.0075	0.0711 ±0.0028	0.1599 ±0.0039	0.0593 ±0.0014	0.1401 ±0.0103	0.0519 ±0.0038
10PPI open-cell foam	0.0197 ±0.0049	0.0910 ±0.0226	0.0144 ±0.0044	0.0668 ±0.0204	0.0130 ±0.0044	0.0603 ±0.0206
20PPI open-cell foam	0.0188± 0.0031	0.0872 ±0.0144	0.0150 ±0.0027	0.0696 ±0.0125	0.0116 ±0.0012	0.0538 ±0.0057
10PPI foam filled with water	0.0880 ±0.0126	0.0775 ±0.0111	0.0692 ±0.0068	0.0609 ±0.0060	0.0615 ±0.0054	0.0541 ±0.0048
20PPI foam filled with water	0.0909 ±0.0084	0.0801 ±0.0074	0.0751 ±0.0076	0.0661 ±0.0067	0.0674 ±0.0014	0.0593 ±0.0013
10PPI foam filled with 2%(w/v) boric acid solution	0.0996 ±0.0077	0.0872 ±0.0067	/		/	

Table 4.13 (continued).

20PPI foam filled with 2%(w/v) boric acid solution	0.1225 ±0.0007	0.1073 ±0.0006	/	/

Table 4.14: Comparison of mass attenuation coefficients between results from measurements and XCOM.

Sample	Mass attenuation coefficient μ/ρ (cm^2g^{-1})					
	0.662 MeV		1.173 MeV		1.332 MeV	
	Expt.	XCOM	Expt.	XCOM	Expt.	XCOM
Pure bulk Al	0.0705 ±0.0007	0.0746	0.0542 ±0.0014	0.0568	0.0491 ±0.0007	0.0533
	Difference: 5.496%		Difference: 4.577%		Difference: 7.880%	
Bulk 6061 Al alloy	0.0711 ±0.0028	0.0746	0.0592 ±0.0014	0.0568	0.0519 ±0.0038	0.0532
	Difference: 4.692%		Difference:4.054%		Difference: 2.444%	
10PPI foam filled with water	0.0775 ±0.0111	0.1387	0.0609 ±0.0060	0.1057	0.0541 ±0.0048	0.0989
	Difference: 44.124%		Difference: 42.384%		Difference: 45.298%	
20PPI foam filled with water	0.0801 ±0.0074	0.1387	0.0661 ±0.0067	0.1057	0.0593 ±0.0013	0.0989
	Difference: 42.25%		Difference: 37.465%		Difference: 40.040%	

Table 4.14 (continued).

10PPI foam filled with 2%(w/v) boric acid solution	0.0872 ±0.0067	0.1377	/	0.1047	/	0.0980
	Difference: 36.674%					
20PPI foam filled with 2%(w/v) boric acid solution	0.1073 ±0.0006	0.1377	/	0.1047	/	0.0980
	Difference: 22.077%					

A graphical comparison is made as shown in Figure 4.8.

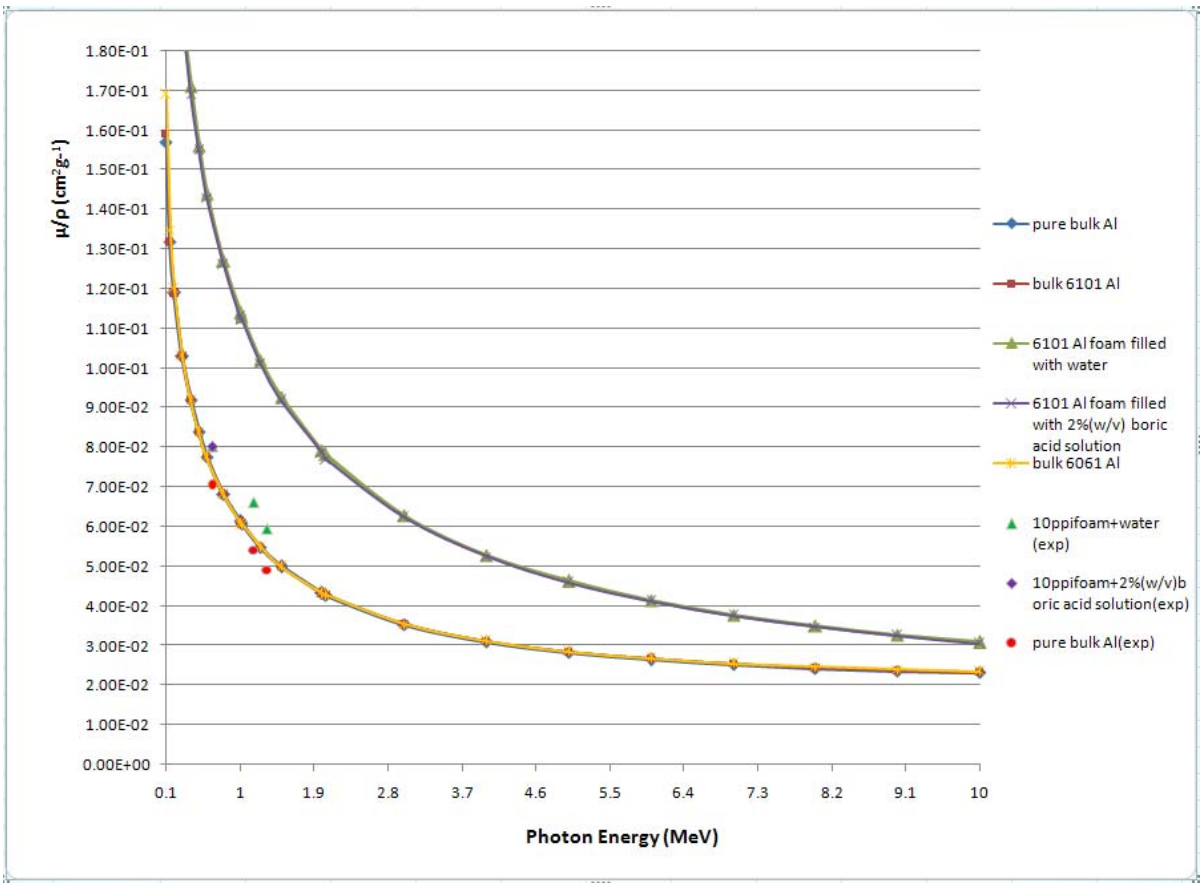

Figure 4.8：Comparison of mass attenuation coefficients for bulk and “foam + liquid” samples.

From Figure 4.8, it is shown that the lines of bulk materials almost overlap each other. For the "foam + liquid" samples, the equivalent total mass attenuation coefficients for the equivalent foam with boric acid solution mixture are a bit lower than the coefficients for the equivalent foam with water mixture. Figure 4.8 illustrates this tendency by a plot of total mass attenuation coefficient vs. photon energy.

The comparison also shows the experimental results for bulk material samples are in good agreement with those given by XCOM.

However, as to "foam + water" and "foam + boric acid solution" samples, large differences between the data obtained from experimental results and XCOM occur at all the three energies. A variety of factors may contribute to the differences:

- First of all, the inherent fluctuations represent an unavoidable source of uncertainty in all measurements, which are associated with the instruments used. One of the sources of uncertainty is the radioactive decay of the source used in counting, which is statistical by nature.
- The total attenuation coefficients for the equivalent mixtures obtained from XCOM were calculated as sums of the corresponding quantities for the atomic constituents, after the fractions by weight of the various components were input. Thus, the "foam + water" and "foam + boric acid solution" samples were treated as equivalent "homogenous mixture" in the XCOM program. The unique structure of the actual foam samples were not taken into account in XCOM. Additionally, the calculation using experimental results treated layers of a certain type of sample as an entire slab and obtained the mass attenuation coefficients.

Then the average values were taken as the data of experimental mass attenuation coefficients. However, the small gap between layers may contribute to the uncertainty and error of measurements.

- Some limitations should be noted. The cross-sections for elements in the XCOM database pertain to isolated neutral atoms, and do not take into account molecular and solid-state effects which modify the cross sections, especially in the vicinity of absorption edges. Relatively small cross-sections, such as those for Delbruck scattering, two-photon Compton scattering or photo-meson production, are not included. Finally, XCOM does not calculate energy absorption coefficients that represent the conversion of photon energy to kinetic energy of secondary Compton-, photo-, and pair-electrons [71].

  Another limitation of XCOM is that it can generate data only for solid materials, but not for the foam samples which contains "void space".

- In fact, the "foam + liquid" samples consist of 6101 Al open-cell foams filled with water or boric acid solution, which are not homogenous. The non-homogeneity of this structure complicates energy loss estimates. The open-cell foam sample does not have a uniform structure inside. The cell wall thickness variation and cell size variation contribute to the non-uniformity of the cellular structure, and additionally contribute to the anisotropic physical properties. These reasons contribute to the difficulty of accurately predicting the fluid distribution inside the pores, making the difference between the real experimental results and assumed "homogeneous" results larger.

However, the experimental and theoretical results still show some similar tendencies in attenuation of gamma-rays at the three photon energies in this work:

- As photon energy increases, the mass attenuation coefficients of all the sample materials decrease.
- The mass attenuation coefficients of the "equivalent" homogenous mixtures predicted by XCOM are larger than those of the bulk materials in the energy range from 0.1 MeV to 10 MeV, as shown in Figure 4.8.

  The same trend can also be observed from the experimental results. For the photon energy of 0.662 MeV, 1.173 MeV and 1.332 MeV, all the "foam + liquid" samples show better attenuation than bulk samples.
- For "foam + liquid" samples, only the lower energy of 0.662 MeV was used to deal with samples filled with boric acid solution. The results show a bit increase of mass attenuation coefficients than those of samples filled with water, while the XCOM data give lower coefficients for samples filled with boric acid solution.

  A reasonable explanation is that the boric acid itself has lower mass attenuation coefficients than water, as shown in Figure 4.9.

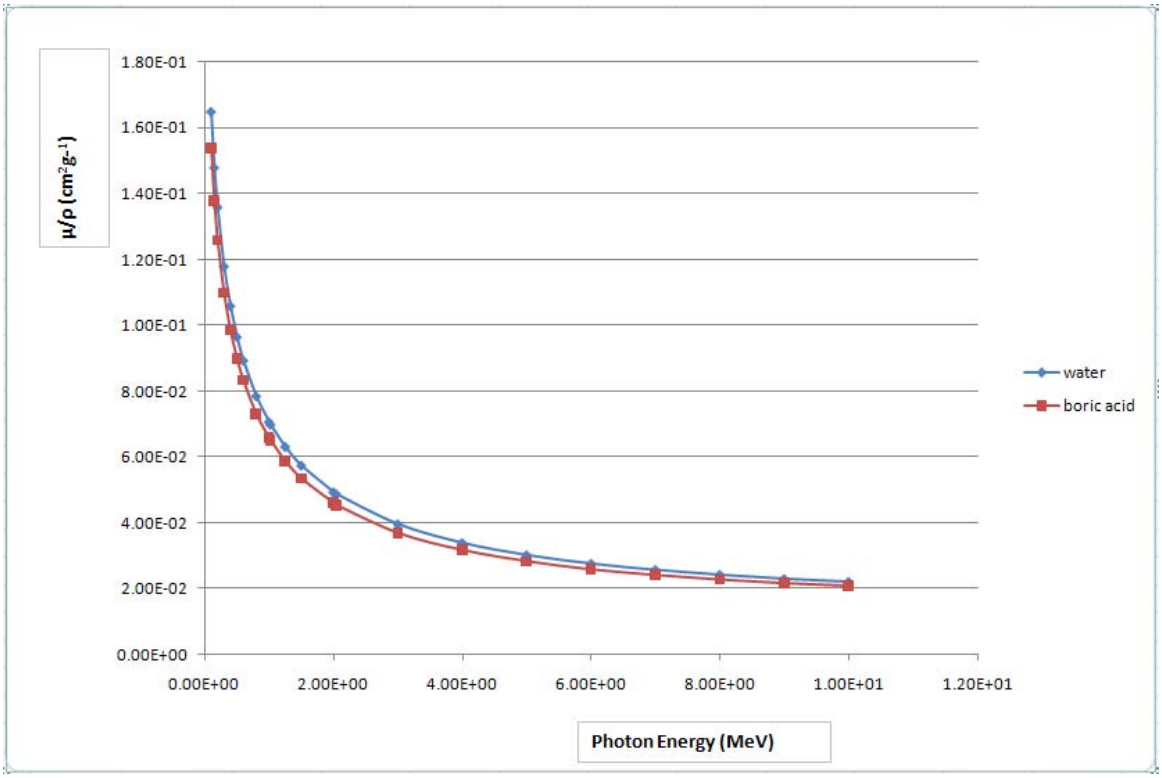

Figure 4.9: Mass attenuation coefficients of water and boric acid.

A conclusion could be drawn from both the XCOM and experimental results are that "foam + liquid" samples do have larger mass attenuation coefficients than bulk samples. Since the mass attenuation coefficients already consider the density factor, definitely we can make a conclusion that the "foam + liquid" samples have better attenuation while having the benefit of weight saving. This point is illustrated in Figure 4.10, which shows a plot of the experimental results for bulk material and "10 PPI foam + water" samples.

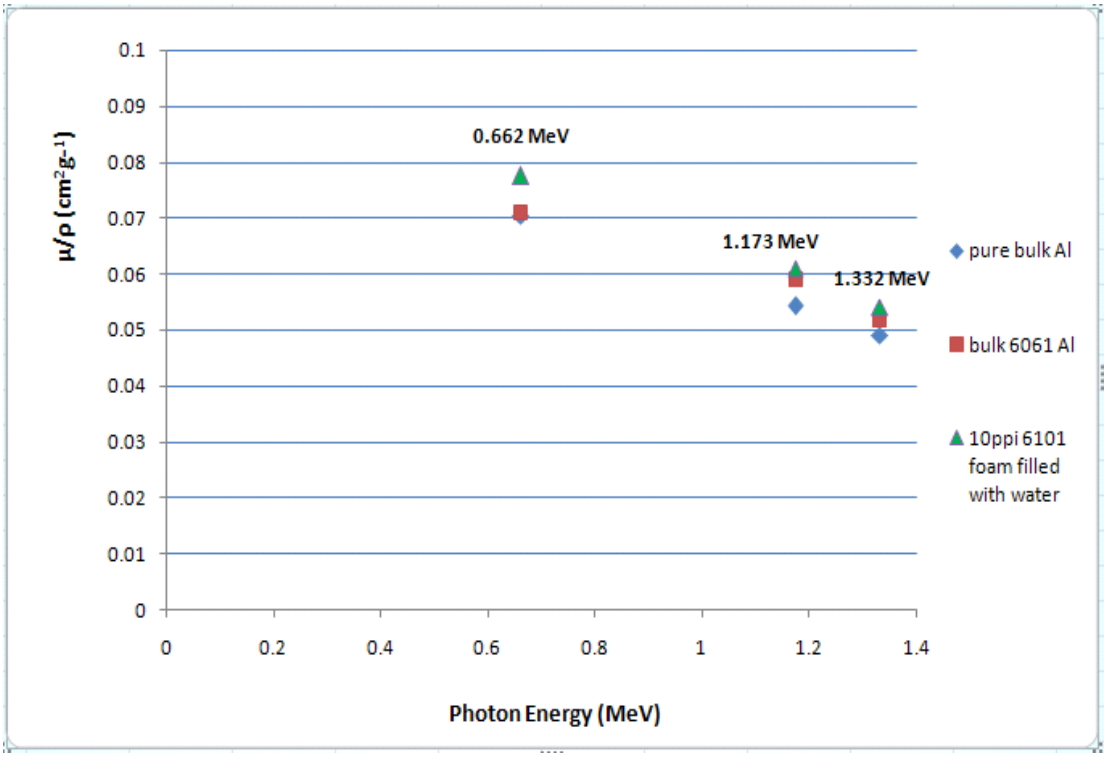

Figure 4.10: Plot of mass attenuation coefficient vs. photon energy of experimental results.

4.2 Neutron Attenuation Results and Discussion

4.2.1 Results from Measurements with the thermal neutron beam

The thermal neutron measurements used four types of samples: pure bulk Al, 10 PPI 6101 Al foam, "foam + water" samples, and "foam ＋boric acid solution" samples. Here, boric acid solutions with three different concentrations were tried in these measurements.

Tables 4.15 to 4.20 list the recorded data of transmitted intensities and relative uncertainties for each single measurement.

Table 4.15: Transmitted intensities and uncertainty for bulk samples in thermal neutron transmission measurements.

I_0= 38444				
Sample Materials	Thickness (inch)	Net Transmitted Intensity (I)	Relative Uncertainty	Transmission ($T=I/I_0$)
Pure bulk Al	0.25	34103	0.54%	0.887
	0.5	31964	0.56%	0.831
	0.75	29854	0.58%	0.777
	1	27722	0.60%	0.721
	1.25	24198	0.64%	0.629
	1.5	23832	0.65%	0.620

Table 4.16: Transmitted intensities and uncertainty for foam samples in thermal neutron transmission measurements.

I_0= 38444				
Sample Materials	Thickness (inch)	Net Transmitted Intensity (I)	Relative Uncertainty	Transmission ($T=I/I_0$)
10PPI open-cell Al foam	0.5	35394	0.53%	0.921
	0.75	33174	0.55%	0.863
	1	30983	0.57%	0.806
	1.25	28770	0.59%	0.748
	1.5	26112	0.62%	0.679

Table 4.17: Transmitted intensities and uncertainty for foam samples filled with water in thermal neutron transmission measurements.

I_0= 38444				
Sample Materials	Thickness (inch)	Net Transmitted Intensity (I)	Relative Uncertainty	Transmission ($T=I/I_0$)
10PPI open-cell Al foam filled with water	0.5	30893	0.57%	0.804
	0.75	29096	0.59%	0.757
	1	26119	0.62%	0.679
	1.25	23526	0.65%	0.612
	1.5	21982	0.67%	0.572

Table 4.18: Transmitted intensities and uncertainty for foam samples filled with 1% (w/v) boric acid solution in thermal neutron transmission measurements.

I_0= 35093				
Sample Materials	Thickness (inch)	Net Transmitted Intensity (I)	Relative Uncertainty	Transmission ($T=I/I_0$)
10PPI open-cell Al foam filled with 1% (w/v) boric acid solution	0.5	942	3.26%	0.027
	0.75	881	3.37%	0.025
	1	675	3.85%	0.019
	1.25	390	5.06%	0.011
	1.5	84	10.91%	0.002

Table4.19: Transmitted intensities and uncertainty for foam samples filled with 2% (w/v) boric acid solution in thermal neutron transmission measurements.

I_0= 35093				
Sample Materials	Thickness (inch)	Net Transmitted Intensity (I)	Relative Uncertainty	Transmission ($T=I/I_0$)
10PPI open-cell Al foam filled with 2% (w/v) boric acid solution	0.5	890	3.35%	0.025
	0.75	842	3.45%	0.024
	1	485	4.54%	0.014
	1.25	351	5.34%	0.010
	1.5	0		0

Table 4.20: Transmitted intensities and uncertainty for foam samples filled with 3% (w/v) boric acid solution in thermal neutron transmission measurements.

I_0= 35345				
Sample Materials	Thickness (inch)	Net Transmitted Intensity (I)	Relative Uncertainty	Transmission ($T=I/I_0$)
10PPI open-cell Al foam filled with 3% (w/v) boric acid solution	0.5	873	3.38%	0.025
	0.75	826	3.48%	0.023
	1	476	4.58%	0.013
	1.25	344	5.39%	0.010
	1.5	0		0

4.2.2 Analyses and Discussion of Experimental Results

From the measurements, the neutron transmission ($T = I_0/I$) can be calculated for different types of samples with different thicknesses.

The neutron total cross section σ(E) is related to the neutron transmission T(E) of a sample of thickness t by

$$T(E) = \exp\{-tN\sigma(E)\} = \exp\{-n\sigma(E)\} \tag{3.2}$$

where the cross-section σ(E) is given in barns (b) and n in atom/barn (at/b). However, the transmission of neutrons through the sample cannot be measured at the precise energy E of the neutrons, but instead is averaged over the width of the experimental resolution function [72]. The quantity actually measured is:

$$T(E) = \int \exp\{-n\sigma_{\Delta}(E')\}R(E - E')dE' \tag{3.3}$$

where R is the experimental resolution function and $\sigma_{\Delta}(E')$ is the Doppler-broadened cross section at energy E' [72].

The so-called effective average total cross-section $\sigma_{eff}(E)$ given by:

$$\sigma_{eff}(E) = -(1/n)\ln(T(E)) \tag{3.4}$$

is smaller than the true average total cross-section σ(E). The difference is due to the resonance structure of the data and is important for thick samples. The effect is negligible if n is small. However, using thin samples will introduce large experimental errors on the cross-section. Usually, large n values are used in the transmission measurements, which make the self-shielding corrections unavoidable [72]. The smallest thickness of the bulk pure aluminum sample used in these transmission measurements is calculated as 0.0383 at/b, which is considered as a large n value.

Direct calculation of the cross-sections for thick samples in this experiment is hardly feasible, especially for the "foam + liquid" samples which are not "homogenous mixtures". On another hand, the unique structure of the foam and "foam + liquid" samples

and the polyenergetic property of the thermal neutron beam complicate the total cross-section calculation. For the purpose of the work in current stage, the transmission (T) was determined from the experimental results and some analyses were made.

A plot of transmission (T) vs. thickness for different types of sample in the thermal neutron transmission measurements is shown in Figure 4.11.

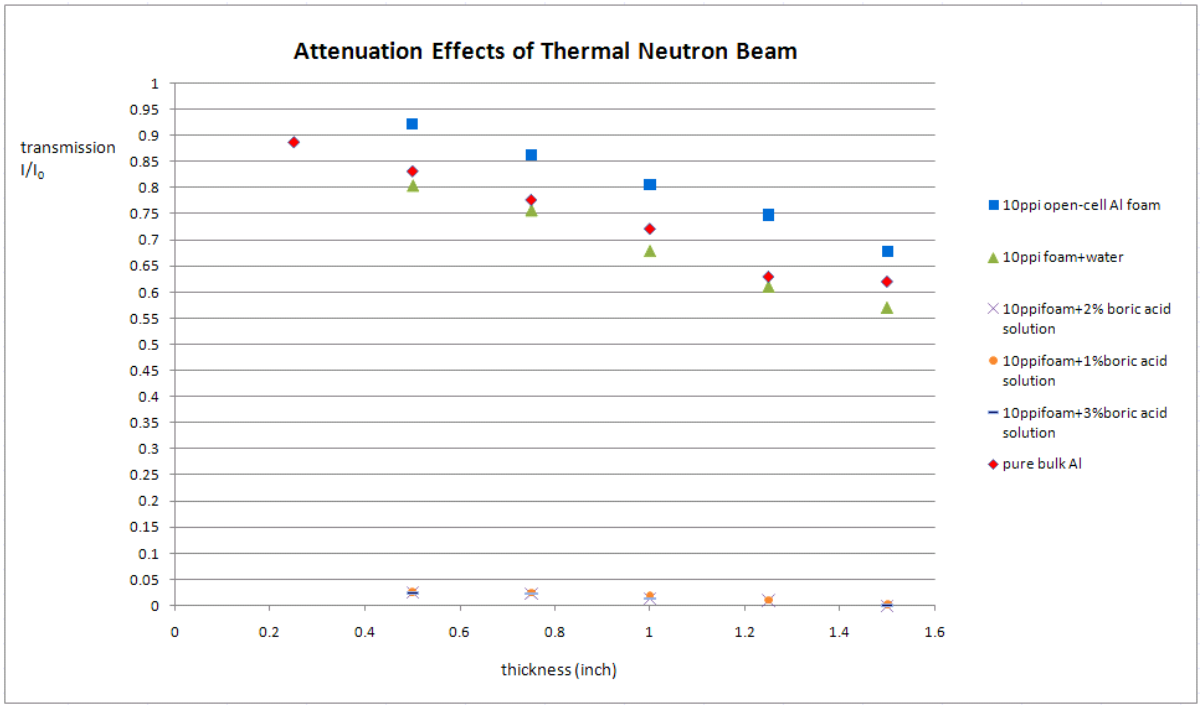

Figure 4.11: Attenuation of samples in the thermal neutron beam.

From Figure 4.11 some conclusions could be drawn as follows:

- For a type of sample at certain energy, the transmission decreases as the thickness of the sample increases, i.e., the attenuation increases as its thickness increases.
- For a certain energy, the comparison of attenuation for samples at a certain thickness

could be illustrated as:

"foam + boric acid solution" sample > "foam +water" sample > bulk material > foam

- For "foam + water" samples, they showed improved attenuation than the bulk samples. The effect of water can be seen because of its high hydrogen content.
- For "foam + boric acid solution" samples, it is shown that they have way better attenuation than all the types of samples.

It is also noticed that as the w/v concentration of boric acid solution increases, the attenuation increases. For the foam samples filled with 2% (w/v) boric acid solution and 3% (w/v) boric acid solution, the samples with thickness of 1.5 inch totally stopped the beam.

This dramatic increase in attenuation could be explained as the effect of boric acid solution contained in the sample. The reason is that the ^{10}B isotope has a high cross-section for absorption of low energy (thermal) neutrons.

Table 4.21 summarizes the beam intensity reduction of all types of samples of different thicknesses.

Table 4.21: Summary of the beam intensity reduction of all the samples.

Thickness (inch)	Samples	Beam Intensity Reduction Factor $(I_0-I)/I$
0.25	Pure bulk Al	0.113
0.5	6101 bulk open-cell Al foam	0.079
	Pure bulk Al	0.169
	6101 bulk open-cell Al foam + water	0.196
	6101 bulk open-cell Al foam + 1%(w/v) boric acid solution	0.973
	6101 bulk open-cell Al foam + 2%(w/v) boric acid solution	0.975
	6101 bulk open-cell Al foam + 3%(w/v) boric acid solution	0.975
0.75	6101 bulk open-cell Al foam	0.137
	Pure bulk Al	0.223
	6101 bulk open-cell Al foam + water	0.243
	6101 bulk open-cell Al foam + 1%(w/v) boric acid solution	0.975
	6101 bulk open-cell Al foam + 2%(w/v) boric acid solution	0.976
	6101 bulk open-cell Al foam + 3%(w/v) boric acid solution	0.977
1	6101 bulk open-cell Al foam	0.194
	Pure bulk Al	0.279
	6101 bulk open-cell Al foam + water	0.321
	6101 bulk open-cell Al foam + 1%(w/v) boric acid solution	0.981
	6101 bulk open-cell Al foam + 2%(w/v) boric acid solution	0.986
	6101 bulk open-cell Al foam + 1%(w/v) boric acid solution	0.987

Table 4.21 (continued).

1.25	6101 bulk open-cell Al foam	0.252
	Pure bulk Al	0.371
	6101 bulk open-cell Al foam + water	0.388
	6101 bulk open-cell Al foam + 1%(w/v) boric acid solution	0.989
	6101 bulk open-cell Al foam + 2%(w/v) boric acid solution	0.99
	6101 bulk open-cell Al foam + 3%(w/v) boric acid solution	0.99
1.5	6101 bulk open-cell Al foam	0.321
	Pure bulk Al	0.380
	6101 bulk open-cell Al foam + water	0.428
	6101 bulk open-cell Al foam + 1%(w/v) boric acid solution	0.998
	6101 bulk open-cell Al foam + 2%(w/v) boric acid solution	1
	6101 bulk open-cell Al foam + 3%(w/v) boric acid solution	1

Chapter 5 Summaries and Recommendations

5.1 Summaries of the Work Done

The goal of this work was to design and test a new structure for nuclear radiation shielding applications using novel metallic foams, in order to meet needs for lightweight multifunctional shielding materials. Two sections of radiation transmission experiments dealing with different radiation sources were designed. Gamma-ray transmission experiment was carried out with three different photon energies. Thermal neutron transmission experiment was done in the NCSU PULSTAR Reactor beam port #5. Multiple measurements were performed and the experimental results were analyzed.

The gamma-ray experiment results shows the metallic foam itself attenuates less gamma-ray compared to bulk material, as a consequence of saving weight. The results also predict a tendency that by filling foam with liquid, the attenuation ability of the sample would be better than the pure bulk material and its base material the foam made from. At the same time it owns the advantage of saving weight. The liquid filled in foam in this work water and boric acid solution. It has been found out to have almost the same effect on attenuating gamma-ray.

The thermal neutron experiment verifies the assumption that the boric acid solution works for attenuating thermal neutron. The results have shown that by filling foam with water or boric acid solution, the attenuation got improved compared to bulk material and foam. Foams filled with boric acid solution have the most obvious attenuating effect. By

increasing the boric acid concentration and thickness of the layers, the samples even totally stopped the beam.

5.2 Recommendations for Future Work

The results of the experiments and analyses throughout this work lead to several different options for future work, which will be discussed below.

- Facility improvements – More radioactive sources could be used to conduct the measurements to test this shielding structure in a wider range of energies. Future work on neutron shielding may include fast neutron sources.
- Application specifications – For this stage no specific type of nuclear radiation shielding application was targeted. This work only aimed at very general application as the first step for developing this novel structure. Potential applications could be spent nuclear fuel cask, radiation protection garment, transportation and space application.
- Material developments – The Doucel open-cell foam samples use in this work were made from 6101 Al alloy. But aluminum is not the only choice, and foams made from other material could be taken into account to deal with different applications, such as lead or steel foam.

Along with a certain application objective, comes design and improved experimental methods or simulation. This kind of shielding system have shown potentials in applications owing to the benefits of increased shielding ability and reduced weight. Some additional

advantages might be increased heat rejection capability, improved mechanical load resistance and energy damping capability.

References

[1] Nicholas Tsoulfanidis, *Measurement and Detectioin of radiation 2 nd edition*, 1995.

[2] F. A. Smith, *A Primer in Applied Radiation Physics*, Queen Mary& Westfield College, London,2000.

[3] J. Kenneth Shultis and Richard E. Faw, *Radiation Shielding*, Dept. of Nuclear Engineering, Kansas State Univ., Manhattan, Kansas 2000.

[4] R.Macian, *Introduction to Radiation Shielding*,16.11.06

[5] http://www.australian-radiation-services.com.au

[6] John R. Lamarsh, Anthony J. Baratta, *Introduction to Nuclear Engineering 3 rd edition*, 2001.(was 3)

[7] Glenn F. Knoll, *Radiation Detection and Measurement, 3 rd edition*.

[8] http://en.wikipedia.org/wiki/Lead_shielding

[9] http://en.wikipedia.org/wiki/Radiation_shielding

[10] A. Khanna, S.S. Bhatti, K.J. Singh, K.S. Thind, *Nucl. Instr. and Meth.* B 114 (1996) 217.

[11] H. Singh, K. Singh, G. Sharma, R. Nathuram, H.S. Sahota, *Nucl. Sci. Eng*. 142(2002) 342.

[12] K. Singh, H. Singh, V. Sharma, R. Nathuram, A. Khanna, R. Kumar, S.S. Bhatti, H.S. Sahota, *Nucl. Instr. Meth. Phys. Res. B* 194 (2002) 1.

[13] H. Singh, K. Singh, G. Sharma, L. Gerward, R. Nathuram, B.S. Lark, H.S. Sahota, A. Khanna, *Phys. Chem. Glasses* 44 (2003) 5.

[14] H. Singh, K. Singh, L. Gerward, K.Singh, H.S. Sahota, R. Nathuram, *Nucl. Instr. Meth. Phys. Res. B* 207 (2003) 257-262.

[15] N. Singh, K. J. Singh, K. Singh, H. Singh, *Nucl. Instr. and Meth B,* 225 (2004) 305.

[16] K. Singh, H. Singh, G. Sharma, L. Gerward, A. Khanna, R. Kumar, R. Nathuram, H.S. Sahota, *Raidiat. Phys. Chem*., 72 (2005) 225.

[17] K. Singh, A. Goel, S. Mohan, A. Arora, G. Sharma, *Nucl. Sci. Eng*. 154 (2006) 1.

[18] N. Singh, K. J. Singh, K. Singh, H. Singh, *Radiat. Measurement*, 41 (2006) 84.

[19] James E. Turner, *Atoms, Radiation, and Radiation Protection, 2 nd edition*

[20] Satish Chandra Gupta, G.L. Baheti, B.P.Gupta, *Radiation Physics and Chemistry* 59 (2000) 103-107

[21] http://en.wikipedia.org/wiki/Boron

[22] http://en.wikipedia.org/wiki/Boric_acid

[23] Shielding Materials, DOE-HDBK-1017/2-93, http://www.tpub.com/content/doe/h1017v2/css/h1017v2_79.htm9

[24] S. Kobayashi, N. Hosoda, and R. Takashima, *Nucl. Instrum. Meth. A390*, 426 (1997).

[25] W.S. Rothwell, *Radiation Shielding Windows Glasses*, Bull, PE-50, Corning Glass Works, Corning, NY, 1958.

[26] L.M. Melnick, H.W. Safford, K.H. Sun, A.J. Silverman, *Am. Ceram, Soc.* 34 (1951) 82.

[27] S. Singh, A. Kumar, D. Singh, K.S. Thind, G.S. Mudahar, *Barium-Borate-Flyash Glasses: As Radiation Shielding Materials, Nucl. Instr. and Meth. In Phys. Res.* B (2007), doi: 10.1016/j. nimb. 2007.10.018.

[28] http://www.boronrubbersindia.in/

[29] Duan Yonghua, Zhu Peixian, Sun Yong, Research of Shielded/Structural Integration B/Pb Composites Structure and Mechanical Properties.

[30] http://en.wikipedia.org/wiki/Metal_foam.

[31] M.F. Ashby, A. Evans, N.A. Fleck, L.J. Gibson, J.W. Hutchinson, H.N.G. Wadley, *Metal Foams: A Design Guide*, Butterworth-Heinemann, Massachusetts, 2000.

[32] C., San Marchi, J.-F. Despois Mortensen *A. Acta Mater*. 52 (2004) 2895.

[33] A. –M., Harte N. A., Fleck and M. F. Ashby Acta Mater. 47 (1999) 2511.

[34] H.P. Degischer, B. Kriszt, Handbook *of Cellular Metals, Production, Processing, Applications*, Wiley-VCH Verlag GMBH, Weinheim, Germany, 2002.

[35] Recemat International, http://www.recemat.com/en/index.html.

[36] Porvair PLC, http://www.porvair.com.

[37] ERG Materials and Aerospce Corporation, http://www.ergaerospace.com.

[38] Inco Special Products Is a A Business Unit of Inco Limited, http://www.incospp.com.

[39] Spectra-Mat, Incorportated, http://www.spectramat.com.

[40] J. Banhart, J. Baumeister, *Materials Research Symposium Proceedings*, Vol.521, pp.121-132, 1998.

[41] O'Neil, Adrian Thomas, *Development of Closed Cell Metallic Foam Using Casting Techniques*, thesis, 2004.

[42] L. J. Gibson, M.F. Ashby, *Cellular Solids, Structure And Properties*, 2nd Edition, Cambridge University Press, Cambridge, UK, 1997.

[43] Fourie, J.G., & Du Plessis, J.P., (2002), *Chem, Eng. Sci*, 57, 2781-2789

[44] Wassim Elias Azzi, *A Systematic Study of the Mechanical and Thermal Properties of Open Cell Metal Foams for Aerospace Applications*, thesis, 2004.

[45] C.Y. Zhao, T.J. Lu, H.P. Hodson, *International Journal of Heat and Mass Transfer* 47 (2004) 2927-2939.

[46] B.P. Neville, A. Rabiei, *Materials and Design* 29 (2008), 388-396.

[47] Lakshmi J. Vendra, A. Rabiei, Material Science and Engineering A 465 (2007) 59-67

[48] J. Banhart, *Progress in Materials Science* 46, pp.559-632, 2001.

[49] http://www.msm.cam.ac.uk/mmc/people/old/dave/.

[50] T. Miyoshi, M. Itoh, S. Akiyama, A. Kitahara, *Adavanced Engineering Materials* 2000, 2, No.4.

[51] http://ergaerospace.com/foamproperties/aluminumproperties.htm

[52] J. Banhart *Prog. Mater. Sci*.46 (2001) 2463.

[53] E. Amsterdam, P.R. Onck, J.TH.M. De Hosson, *Journal of Materials Science* 40 (2005) 5813-5819.

[54] J., Zhou C., Mercer W.O. Soboyejo *Met. Trans*. 33A (2002) 1413.

[55] James E. Turner, Atoms, Radiation, and Radiation Protection, 2nd Edition, 1995

[56] Julian Cassa, http://mightylib.mit.edu

[57]R.D. Evans, The Atomic Nucleus, McGraw-Hill Book Co., New York, 1955.

[58] G. Nelson and D. Reilly, *Gamma-Ray Interactions with Matter,*

http:// www.fas.org/sgp/othergov/doe/lanl/lib-www/la-pubs/00326397.pdf.

[59] Canberra Genie 2000 Operations Manual.

[60] Nuclear Science Exp. II-Beta, Gamma Interaction.

[61] Gurdeep S. Sidhu, Karamjit Singh, Parjit S. Singh, Gurmel S. Mudahar, *Radiation Physics and Chemistry* 56 (1999) 535-537.

[62] http://en.wikipedia.org/wiki/NCSU_Reactor_Program

[63] Savvas Morris, *Calibration and Evaluation of the Prompt Gamma Activation Analyssis Facility at the NCSU PULSTAR Nuclear Reactor for Boron Neutron Capture Therapy Purposes*, thesis, 1996.

[64] C. W. Mayo, K. Verghese, Y. G. Huo, Mixed Enrichment Core Design for the NC State University PULSTAR Reactor, report of DOE/NE/38004../ 1997.

[65] Kaushal Kishor Mishra, *Development of a Thermal Neutron Imaging Facility at the NC State University PULSTAR reactor*, thesis, 2005.

[66] R. Berliner, et al., "*Hardware and Software System Design for High Resolution Linear Position Sensitive Proportional Counter Detector Arrays*", Proceedings of the International Workshop on Data Acquisition Systems for Neutron Experimental Facilities, Frank Laboratory of Neutron Physics, 1997

[67] Canberra doc. Neutron Detection and Counting

[68] http://www.amptek.com/mca8000a.html

[69] K.H. Beckurts, K. Wirtz, Neutron Physics, Springer-Verlag, 1964

[70] http://en.wikipedia.org/wiki/Thermal_neutron

[71] http://physics.nist.gov/PhysRefData/Xcom/Text/XCOM.html

[72] Herve Derrien, Klaus H. Guber, John A. Harvey, Nancy M. Larson and Luiz C. Leal, *Average Total Cross Sectin of 233U, 235U and 239Pu from ORELA Transmission*

Measurements and Statistical Analysis of the Data, Oak Ridge National Laboratory, Manuscript 149.